The Astrophysical Journal, 927:213 (19pp), 2022 March 10 https://doi.org/10.3847/1538-4357/ac4e7d
© 2022. The Author(s). Published by the American Astronomical Society.
OPEN ACCESS

Methanol Mapping in Cold Cores: Testing Model Predictions*

Anna Punanova[1], Anton Vasyunin[1], Paola Caselli[2], Alexander Howard[3], Silvia Spezzano[2], Yancy Shirley[4], Samantha Scibelli[4], and Jorma Harju[5,2]
[1] Ural Federal University, 620002, 19 Mira street, Yekaterinburg, Russia; anna.punanova@urfu.ru, punanovaanna@gmail.com
[2] Max-Planck-Institut für extraterrestrische Physik, Giessenbachstrasse 1, D-85748 Garching, Germany
[3] School of Physics and Astronomy, Cardiff University, 5 The Parade, Cardiff CF24 3AA, UK
[4] Steward Observatory, University of Arizona, Tucson, AZ 85721, USA
[5] Department of Physics, University of Helsinki, P.O. Box 64, FI-00014, Finland
Received 2021 October 8; revised 2021 November 26; accepted 2021 December 8; published 2022 March 17

Abstract

Chemical models predict that in cold cores gas-phase methanol is expected to be abundant at the outer edge of the CO depletion zone, where CO is actively adsorbed. CO adsorption correlates with volume density in cold cores, and, in nearby molecular clouds, catastrophic CO freeze-out happens at volume densities above 10^4 cm^{-3}. The methanol production rate is maximized there and its freeze-out rate does not overcome its production rate, while the molecules are shielded from UV destruction by gas and dust. Thus, in cold cores, methanol abundance should generally correlate with visual extinction, which depends on both volume and column density. In this work, we test the most basic model prediction that maximum methanol abundance is associated with a *local* $A_V \sim 4$ mag in dense cores and constrain the model parameters with the observational data. With the IRAM 30 m antenna, we mapped the CH_3OH (2–1) and (3–2) transitions toward seven dense cores in the L1495 filament in Taurus to measure the methanol abundance. We use the Herschel/SPIRE maps to estimate visual extinction, and the $C^{18}O$(2–1) maps from Tafalla & Hacar to estimate CO depletion. We explored the observed and modeled correlations between the methanol abundances, CO depletion, and visual extinction, varying the key model parameters. The modeling results show that hydrogen surface diffusion via tunneling is crucial to reproduce the observed methanol abundances, and the necessary reactive desorption efficiency matches the one deduced from laboratory experiments.

Unified Astronomy Thesaurus concepts: Star forming regions (1565); Interstellar molecules (849); Molecule formation (2076); Submillimeter astronomy (1647); Astrochemistry (75)

Supporting material: data behind figures, tar.gz file

1. Introduction

Methanol is a key precursor for many complex organic and prebiotic molecules found in regions of star and planet formation and thus it is very important for the growth of molecular complexity in the interstellar medium (ISM). It is observed at all stages of star formation, including the dense cold molecular gas within starless cores, characterized by temperatures of $T \simeq 10$ K, gas densities $n(H_2) > 10^4$ cm^{-3}, and subsonic turbulence (e.g., Benson & Myers 1989; Bergin & Tafalla 2007; Keto & Caselli 2008). Geppert et al. (2006) showed that gas-phase synthesis cannot account for the observed amounts of methanol in the cold gas, which implies that chemical processes on interstellar dust grains must play the major role in the formation of this molecule. Indeed, the laboratory studies by Watanabe & Kouchi (2002) and Fuchs et al. (2009) confirmed that methanol can be formed efficiently during the hydrogenation of CO molecules on surfaces of interstellar dust analogs at temperatures of ∼10 K. Once formed, some of the solid methanol is delivered from cold grains to the gas phase, where it is widely observed. The delivery mechanism is not well understood. In cold dark star-forming clouds, methanol is most likely delivered to the gas phase via the so-called reactive desorption mechanism (Garrod et al. 2007; Minissale et al. 2016; Chuang et al. 2018). During reactive desorption events, a fraction of the energy released in exothermic surface reactions is spent by the formed molecule to overcome the van der Waals force that binds it to the surface; in this way, reactive desorption occurs. The efficiency of reactive desorption, i.e., the probability that a reaction product will be released to the gas, depends on a number of factors including the exothermicity of a reaction, the properties of the underlying surface etc. Existing studies report very different values of the efficiency of reactive desorption for species and surfaces, including methanol and other products of CO hydrogenation (see, e.g., Garrod et al. 2007; Vasyunin & Herbst 2013a; Minissale et al. 2016; Fredon et al. 2017; Vasyunin et al. 2017; Wakelam et al. 2017). Unlike water ice mantles, surfaces rich in CO and CH_3OH are necessary for efficient reactive desorption, as found by Minissale et al. (2016). Observations of cold dense cores show strong depletion of CO molecules from the gas phase (Willacy et al. 1998; Caselli et al. 1999; Crapsi et al. 2005; Pagani et al. 2007). CO molecules efficiently freeze out on cold dust grains, thus making them efficient chemical reactors producing methanol and other products of hydrogenation of carbon monoxide. Given the dynamical quiescence and near-spherical geometry of prestellar cores, one can utilize them as

* This work is based on observations carried out under projects 013-18, 125-18, and 031-19 with the IRAM 30 m telescope. Institut de Radioastronomie Millimétrique (IRAM) is supported by INSU/CNRS (France), MPG (Germany), and IGN (Spain).

Original content from this work may be used under the terms of the Creative Commons Attribution 4.0 licence. Any further distribution of this work must maintain attribution to the author(s) and the title of the work, journal citation and DOI.

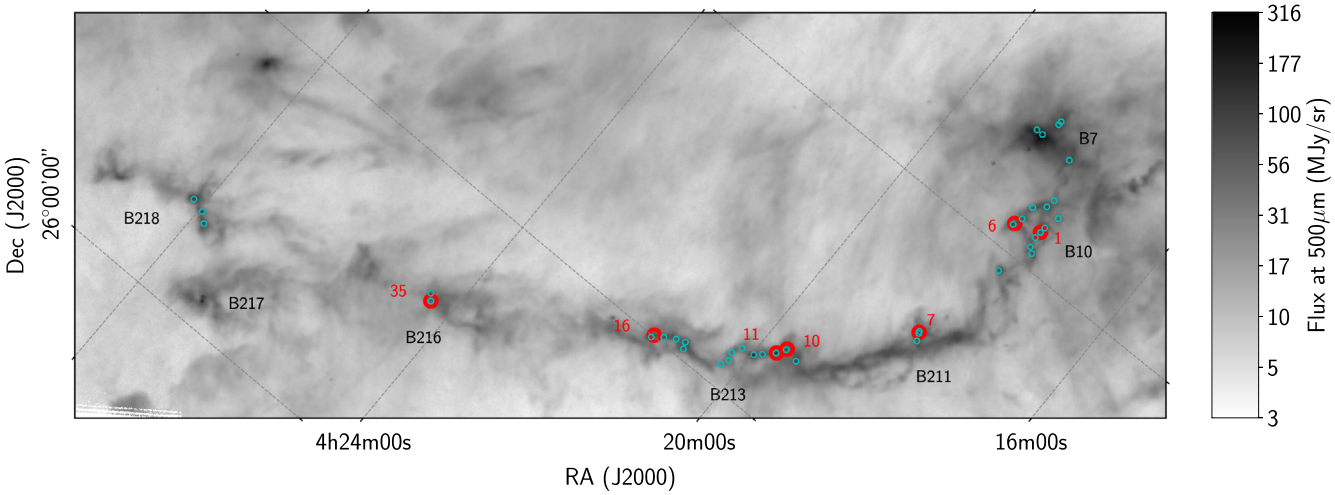

Figure 1. 500 μm dust continuum emission toward the L1495 filament of the Taurus molecular cloud mapped by Herschel/SPIRE (Palmeirim et al. 2013). The cyan circles show the 31 cores observed in methanol by Scibelli & Shirley (2020). Red numbered dots show the dense cores mapped in methanol in this work. We refer to the cores in this work according to these numbers (see Table 1).

natural laboratories to study the poorly known details of methanol formation and its link to carbon monoxide.

Methanol emission toward cold dense cores is observed in integrated intensity maps as ring-like structures (see, e.g., Tafalla et al. 2006; Bizzocchi et al. 2014; Punanova et al. 2018b; Harju et al. 2020; Spezzano et al. 2020) or a single peak toward the core center (Nagy et al. 2019) if the cores have not experienced substantial CO freeze-out, maybe because of their relative dynamical youth compared to other dense cores. Methanol distribution within the ring-like structures is often inhomogeneous (see, e.g., Bizzocchi et al. 2014; Harju et al. 2020). Jiménez-Serra et al. (2016) showed that abundances of methanol and other complex organic molecules (COMs) in the L1544 prestellar core are higher in the shell of the core, which corresponds to $A_V \sim 7.5$–8 mag (see also Vastel et al. 2014). The model, presented in Vasyunin et al. (2017), predicts that the maximal gas-phase abundance of the organic species is at $A_V \sim 8$ mag. Scibelli & Shirley (2020) presented a methanol survey toward the L1495 filament and detected methanol down to the line-of-sight $A_V = 3$ mag, with the 70″ beam of the Arizona Radio Observatory 12 m antenna. In this work, we first test the most basic model prediction that maximum methanol abundance is associated with $A_V \simeq 8$ mag on the line of sight in dense cores (i.e., a local A_V within the core of $\sim$4 mag). Second, we attempt to put observational constraints on the parameterizations of reactive desorption used in chemical models of prestellar cores. The advantage of this study is the wealth of spatial data from high-resolution mapping of seven dense cores embedded within the same filament L1495. This allowed us to constrain model parameters on a multitude of data points, in contrast to a number of previous studies.

The targets of our study are the cold cores in the well studied filamentary structure L1495 in the Taurus molecular cloud (Lynds 1962), which is a nearby (130–135 pc distant; Schlafly et al. 2014; Roccatagliata et al. 2020), quiescent low-mass star-forming region. The filament contains tens of dense cores (Marsh et al. 2014), and about 50 low-mass protostars in different evolutionary stages (Rebull et al. 2010). Hacar et al. (2013) and Seo et al. (2015) note that some parts of the filament are young (B211 and B216) and others (B213 and B7) are more evolved and actively star-forming, based on the number of embedded protostars, their class, and the level of gas turbulence. The dense cores embedded in the filament were detected in N_2H^+ (Hacar et al. 2013), dust continuum emission (Marsh et al. 2014), and ammonia (Seo et al. 2015). The dense cores show a low gas temperature, decreasing toward their centers (8–12 K; Seo et al. 2015), subthermal gas motions (Seo et al. 2015; Punanova et al. 2018a), coherent velocity structure, and slow rotation (Punanova et al. 2018a). The recent observations of the methanol lines at 96.7 GHz toward 31 starless cores detected by Seo et al. (2015) show weaker detections of methanol toward the more evolved regions, and the highest methanol gas abundance in the outskirts of dense gas in B211 (Scibelli & Shirley 2020).

This paper presents maps of methanol lines at 2 and 3 mm toward seven dense cores in the L1495 filament to study the chemical connection between gas-phase methanol, visual extinction, and CO depletion in molecular clouds. We use the observational results to constrain free parameters of the chemical model by Vasyunin et al. (2017) and test the model predictions. In Section 2, we present the details of observations and data reduction. In Section 3, we present the results of methanol column density measurements, abundance estimations, CO depletion, and estimations of molecular hydrogen and visual extinction, and describe the chemical modeling. In Section 5 we discuss the results and correlations between methanol abundance, visual extinction, and CO depletion, and we compare with the results of the chemical model in order to constrain the model parameters. The conclusions are given in Section 6.

2. Observations and Data Reduction

We mapped six methanol lines at 96.7 GHz and 145.1 GHz toward seven dense cores of the L1495 filamentary structure (see Figure 1 and Tables 1 and 2) with the IRAM 30 m telescope (IRAM projects 013-18, 125-18, and 031-19). The observations were performed on 2018 October 17–23, 2019 March 27–29, and 2019 September 16 under acceptable weather conditions, with precipitable water vapor $pwv = 1$–10 mm. The on-the-fly maps were obtained with the EMIR 090 (3 mm band) and EMIR 150 (2 mm band) eight-mixer heterodyne receivers[6] in position switching mode and the VESPA (Versatile Spectrometer Assembly) backend. The spectral resolution was 20 kHz;

[6] http://www.iram.es/IRAMES/mainWiki/EmirforAstronomers

Table 1
The Mapped Cores

Core		α_{J2000}	δ_{J2000}	Region
H2013	S2015	(^{h} ^{m} ^{s})	($^\circ$ $'$ $''$)	
1	12, 13, 14	04:17:42.347	28:07:30.88	B10
6	8, 9	04:18:06.379	28:05:34.87	B10
7	19	04:18:11.343	27:35:33.07	B211
10	22	04:19:36.768	27:15:32.00	B213
11*	23*	04:19:42.154	27:13:31.03	B213
16	33	04:21:20.595	27:00:13.63	B213
⋯	35	04:24:20.600	26:36:02.00	B216

Note. The numbers are given according to Hacar et al. (2013: H2013) and Seo et al. (2015: S2015). The given coordinates are the central positions of the maps. The only protostellar core is indicated with an asterisk (*). The region names are given according to Barnard (1927).

the corresponding velocity resolutions were $\simeq$0.06 km s^{-1} for the 3 mm band and $\simeq$0.04 km s^{-1} for the 2 mm. The beam sizes were $\simeq$26″ for the 3 mm band and $\simeq$17″ for the 2 mm. The system temperatures were 90–627 K depending on the frequency.

The exact line frequencies, beam efficiencies, beam sizes, spectral resolutions, and sensitivities are given in Table 2. Sky calibrations were obtained every 10–15 minutes. Reference positions were chosen individually for each core to make sure that the positions were free of any methanol emission. Pointing was checked by observing QSO B0316+413, QSO B0439+360, QSO B0605-085, Uranus, Mars, or Venus every 2 hr and focus was checked by observing QSO B0439+360, Uranus, Mars, or Venus every 6 hr.

The data reduction up to the stage of the convolved spectral data cubes was performed with the GILDAS/CLASS package.[7] All data were convolved to the 26.″8 beam with the 8.″7 pixel, which is consistent with Nyquist sampling, for consistency of the data set.[8] The following spectral analysis was performed with the Pyspeckit module of Python (Ginsburg & Mirocha 2011).

Four out of six observed lines were detected with signal-to-noise ratio S/N > 5 toward all seven cores. Two lines with the highest energy of the upper level ($E_{up} \simeq 20$ K) were detected only toward the brightest areas of core 1. Therefore these two lines were not used for the analysis and only used to test our method of column density measurement (see Section 3.4 and Appendix A).

3. Results of Observations

To test the model predictions, we apply the most widely used approaches to estimate A_V, CO depletion, and methanol abundance and use the most common data so that our results can be compared easily with other works. We chose to use the Herschel[9] dust continuum emission to measure the column density of molecular hydrogen $N(H_2)$ along with the conversion factor connecting $N(H_2)$ and A_V, since the Herschel survey covered the majority of the selected molecular clouds. To measure the methanol column densities we chose the brightest 2 mm and 3 mm methanol lines. Based on the total nuclear spin of the hydrogen atoms in the methyl group, methanol can take *A*- and *E*-forms. Once formed, *A*- and *E*-methanol molecules keep their hydrogen spines. The ratio of *A*:*E* methanol depends on the temperature at which methanol was formed, with *A*:*E* = 1:1 at 30–40 K and increasing at lower temperatures (see, e.g., Wirström et al. 2011). At the temperatures of our cores, 10–12 K, the *A*:*E* ratio should be $\simeq$1.3. In our observational set, we have only two lines of each methanol form, which is not enough to measure column densities via rotational diagrams robustly, so we combine them and assume a 1:1 *A*:*E* methanol ratio. Besides that, Bizzocchi et al. (2014) found $A{:}E = 1.03 \pm 0.26$ in another Taurus core, L1544.

To measure the column densities of both methanol and CO we assumed the lines are consistent with local thermodynamic equilibrium (LTE) and optically thin emission (which is justified, see Sections 3.2 and 3.4 for details). We also use a large homogeneous data set of typical dense cores in a low-mass star-forming region. To measure T_{dust} and $N(H_2)$ we used the data from the Herschel Spectral and Photometric Imaging Receiver, SPIRE (Palmeirim et al. 2013). To trace CO depletion, we used the $C^{18}O$(2–1) observations by Tafalla & Hacar (2015). We then used $N(H_2)$ to measure the CO and methanol abundances. These steps are described in the following section.

3.1. H_2 Column Density and A_V

The Herschel space telescope carried out the most extensive coverage of dust continuum emission from the molecular clouds in our Galaxy, with PACS[10] and SPIRE instruments. The Herschel science archive is the main source now for the dust continuum emission data in the submillimeter range to estimate dust temperature and molecular hydrogen column densities in molecular clouds (see, e.g., André et al. 2014; Friesen et al. 2017; Ladjelate et al. 2020).

We use the archive Herschel/SPIRE 250, 350, and 500 μm dust continuum emission map (Palmeirim et al. 2013) downloaded from the Herschel Science Archive (Observation ID 1342202254) to measure molecular hydrogen column density $N(H_2)$, visual extinction A_V, and dust temperature T_{dust}. We smooth the 250 and 350 μm maps to the largest beam (of 500 μm) of 38″ and fit a modified blackbody function. We use emissivity index $\beta = 2.0$, typical for starless cores (Draine & Li 2007; Schnee et al. 2010), close to the value $\beta = 2.4$ previously found toward prestellar cores L1544 and Miz-2 in Taurus (Bracco et al. 2017; Chacón-Tanarro et al. 2017). We use dust opacity $\kappa_{250\mu m} = 0.144$ cm^2 g^{-1} based on $\kappa_\nu = 0.1(\nu/10^{12}[\mathrm{Hz}])^\beta$ cm^2 g^{-1} (Beckwith et al. 1990).

To measure visual extinction A_V, we scale H_2 column density following the conversion factor given in Güver & Özel (2009):

$$A_V = \frac{N(\mathrm{H_2})[\mathrm{cm^{-2}}]}{1.105 \times 10^{21}[\mathrm{cm^{-2}/mag}]}. \quad (1)$$

Our peak values of H_2 column density agree within the errors or differ by 20% with those measured by Seo et al. (2015) using the 500 μm Herschel/SPIRE data only (see the comparison of the peak values in Table 3). To evaluate our H_2 column densities with an independent method, we scaled the

[7] Continuum and Line Analysis Single-Dish Software http://www.iram.fr/IRAMFR/GILDAS.

[8] The spectral cubes are available to download as 14 .fits files compressed to one .tar.gz package.

[9] Herschel is an ESA space observatory with science instruments provided by European-led Principal Investigator consortia and with important participation from NASA.

[10] Photodetector Array Camera & Spectrometer.

Table 2
Methanol Lines Observed in This Study

Transition	Frequency[a] (GHz)	E_{up}/k[a] (K)	A[a] (10^{-5} s^{-1})	n_{crit}[c] (10^5 cm^{-3})	F_{eff}	B_{eff}	Δv_{res} (km s^{-1})	rms in T_{mb} (K)	T_{sys} (K)
$(2_{1,2}-1_{1,1})$-E_2	96.739362	12.53[b]	0.2558	0.82	0.95	0.80	0.06	0.08–0.17	70–100
$(2_{0,2}-1_{0,1})$-A^+	96.741375	6.96	0.3408	1.09	0.95	0.80	0.06	0.08–0.17	70–100
$(3_{1,3}-2_{1,2})$-E_2[d]	145.097370	19.51	1.0957	2.74	0.93	0.73	0.04	0.06–0.14	100–160
$(3_{0,3}-2_{0,2})$-A^+	145.103152	13.93	1.2323	13.2	0.93	0.73	0.04	0.06–0.14	100–160
$(2_{0,2}-1_{0,1})$-E_1	96.744550	20.08[b]	0.3407	1.09	0.95	0.80	0.06	0.08–0.17	70–100
$(3_{0,3}-2_{0,2})$-E_1	145.093760	27.1	1.2314	103	0.93	0.73	0.04[e]	0.06–0.14	100–160

Notes.
[a] The methanol 3 mm and 2 mm frequencies, 3 mm energies, and Einstein coefficients are taken from Bizzocchi et al. (2014) following Xu & Lovas (1997) and Lees & Baker (1968), and are also available at the Jet Propulsion Laboratory (JPL) database (Pickett et al. 1998).
[b] Energy relative to the ground $0_{0,0}$, A rotational state.
[c] The critical densities are calculated for a kinetic temperature of 10 K with an assumption of optically thin lines.
[d] The parameters for the 2 mm methanol lines are taken from the JPL database (frequencies and energies, Pickett et al. 1998) and Leiden Atomic and Molecular Database, LAMDA (Einstein coefficients, Schöier et al. 2005).
[e] The 2 mm methanol lines for cores Hacar01, Hacar11, and Seo35 were observed with the Fast Fourier Transform Spectrometer FTS 50 backend with spectral resolution of 50 kHz or 0.10 km s^{-1}. The transitions with $E_{up}/k > 20$ K (below the horizontal line) were not detected in the majority of the cores and were not used in the analysis (see Section 3.2.2 for details).

Table 3
Peak Column and Volume Densities of H_2 toward the Studied Cores

Core	$N(H_2)$ (10^{22} cm^{-2})			$n(H_2)$ (10^5 cm^{-3})			
	SED	S10^N	S15	Here	S10^n	M14	WT16
1	2.65	2.16	$2.53^{+0.19}_{-0.07}$	1.50	⋯	26	0.69
6	2.57	3.21	$2.64^{+0.17}_{-0.27}$	1.39	⋯	6.8	0.81
7	2.40	⋯	$2.21^{+0.28}_{-0.28}$	0.78	⋯	1.9	0.40
10	2.07	2.26	$1.71^{+0.15}_{-0.10}$	0.85	0.18	1.6	⋯
11	2.50	1.23	$2.05^{+0.08}_{-0.07}$	1.83	0.18	⋯	⋯
16	2.80	2.80	$2.38^{+0.21}_{-0.10}$	1.57	0.14	⋯	⋯
35	1.60	3.16	$1.73^{+1.59}_{-0.36}$	0.51	0.17	⋯	⋯

Note. Columns: SED—our $N(H_2)$ based on a modified blackbody spectral energy distribution (SED); S10^N—$N(H_2)$ based on conversion of A_V from Schmalzl et al. (2010); S15—$N(H_2)$ from Seo et al. (2015); Here—$n(H_2)$ modeled in this work; S10^n—$n(H_2)$ from Schmalzl et al. (2010); M14—$n(H_2)$ from Marsh et al. (2014); WT16—$n(H_2)$ from Ward-Thompson et al. (2016).

A_V map of L1495 by Schmalzl et al. (2010) to $N(H_2)$ using the relation (1). In general, the column densities agree within 20% and differ by a factor of two in cores 11 and 35. The difference is not systematic (see the peak values in Table 3 and the comparison of all available points in Figure 13). The A_V map by Schmalzl et al. (2010) was obtained by infrared photometric observations of background stars, so it suffers from gaps and interpolation effects; for example, there are two gaps covering a large area of core 35 and a gap toward core 11—those might have led to the difference of a factor of 2 in the estimated $N(H_2)$. Thus we chose to use the Herschel data to measure both $N(H_2)$ and A_V.

3.2. CO Depletion Factor

In cold, dense, quiescent gas, CO freezes out onto dust grains and some of it is transformed into methanol. The level of CO freeze-out is thus one of the major factors affecting methanol formation (e.g., Whittet et al. 2011). It is commonly expressed as a CO depletion factor, f_d, which is defined as the ratio of the reference maximum abundance of CO (X_{ref}(CO)) in the cloud to the abundance of CO measured in the gas phase in the region of interest, X(CO). CO depletion is also often used as a chemical age indicator that helps to link the observed molecular abundances to the modeled ones (e.g., Jiménez-Serra et al. 2016; Lattanzi et al. 2020).

To measure the gas-phase CO abundance toward the cores, we use the C^{18}O(2–1) maps obtained with the IRAM 30 m antenna, convolved to 23″ beam, by Tafalla & Hacar (2015),[11] except for core 35, which belongs to the B216 region; there is no published C^{18}O(2–1) map for B216. X_{ref}(CO) is defined in Section 3.2.2.

3.2.1. $C^{18}O$ Column Densities

Tafalla & Hacar (2015) find more than one C^{18}O line velocity component toward many positions in their map. Some of these components belong to the dense cores; the others belong to their envelopes or other material in the molecular cloud on the line of sight. Hacar et al. (2013) and Tafalla & Hacar (2015) resolve and analyze the material as small fibers composing the bigger filament. Since the molecular hydrogen column densities measured both via A_V and via dust continuum emission do not contain kinematic information, we integrate all emission in the C^{18}O(2–1) spectra to measure the integrated intensity W and column density N_{tot}.

To measure the C^{18}O column densities, we assume that the C^{18}O(2–1) lines are optically thin and consistent with LTE. Following Caselli et al. (2002), the column density is then

$$N_{tot} = \frac{8\pi W}{\lambda^3 A_{ul}} \frac{g_l}{g_u} \frac{1}{J_\nu(T_{ex}) - J_\nu(T_{bg})} \frac{1}{1 - \exp(-h\nu/kT_{ex})} \times \frac{Q_{rot}}{g_l \exp(-E_l/kT_{ex})}, \quad (2)$$

where A_{ul} is the Einstein coefficient, g_l and g_u are the statistical weights of the upper and lower levels, λ is the wavelength, $J_\nu(T)$ is the equivalent Rayleigh–Jeans temperature, $T_{bg} = 2.7$ K is the

[11] The data are available via Strasbourg astronomical Data Center (CDS): https://cdsarc.cds.unistra.fr/ftp/J/A+A/574/A104/.

Table 4
CO Depletion with Different $X_{ref}(C^{18}O)$

$X_{ref}(CO)$	$X_{ref}(C^{18}O)$	f_d			$N(f_d<1)$		Citation	Also used in
		min.	median	max.				
$0.39\times10^{-4*}$	0.7×10^{-7}	0.04	0.36	5.9	15,954	70%	Tafalla & Santiago (2004)	
0.85×10^{-4}	1.7×10^{-7}	0.09	0.87	14.4	8639	38%	Frerking et al. (1982)	Bacmann et al. (2002)
							Alonso-Albi et al. (2010)	Jørgensen et al. (2002)
								Crapsi et al. (2005)
1.7×10^{-4}	3.0×10^{-7}[a]	0.17	1.54	25.5	4675	20%	Lacy et al. (2017)	
$2.7^{+6.4}_{-1.2}\times10^{-4}$	4.8×10^{-7}[a]	0.27	2.47	40.8	1625	7%	Lacy et al. (1994)	Lee et al. (2003)

Note.
[a] Abundances found by applying the fractional abundance $^{16}O/^{18}O = 560$ from Wilson & Rood (1994).

cosmic background temperature, T_{ex} is the excitation temperature, and E_l is the energy of the lower level. The partition function Q_{rot} of linear molecules (such as CO) is given by

$$Q_{rot} = \sum_{J=0}^{\infty}(2J+1)\exp(-E_J/kT), \quad (3)$$

where J is the rotational quantum number, $E_J = J(J+1)hB$, and B is the rotational constant. We assume $T_{ex} = 10$ K, which is consistent with the gas temperature measured by Seo et al. (2015). With $T_{ex} = 10$ K, Equation (2) for the $C^{18}O(2–1)$ line can be simplified to $N_{tot} \simeq 6.528\times10^{14}W$, where W is in K km s^{-1} and N_{tot} is in cm^{-2}.

The excitation conditions of $C^{18}O$ are close to those of the main isotopologue CO. The optically thin critical density of the $C^{18}O(2–1)$ transition is 2×10^4 cm^{-3}, such that at lower densities it would deviate from LTE. With the statistical equilibrium radiative transfer code RADEX, we estimated that $T_{ex} \simeq 5$ K only toward the less dense outskirts of the cores ($n \sim 10^3$ cm^{-3}), which gives N_{tot} twice as high as that with LTE at 10 K.

3.2.2. CO Depletion: Choice of the Reference CO Abundance

The reference abundance of CO with respect to H_2 in the local ISM has been estimated in a number of studies with a spread between 0.4×10^{-4} and 2.7×10^{-4} (Wannier 1980; Frerking et al. 1982; Lacy et al. 1994; Tafalla & Santiago 2004). The numbers given in the literature are presented in Table 4.

To choose the reference abundance of CO from the values given in Table 4, we calculated CO depletion factors for each data point of the entire $C^{18}O(2–1)$ map of the L1495 filament provided in Tafalla & Hacar (2015) (B7, B10, B211, B213, B218). The area mapped by Tafalla & Hacar (2015) reaches the relatively diffuse outskirts of the filament, where CO should be undepleted. By definition, the depletion factor must be equal to unity there: $f_d = 1$. Thus, our goal is to find the reference abundance of CO that provides the value of f_d close to unity in the diffuse outskirts of the filament, and also ensures the minimum number of data points in the $C^{18}O(2–1)$ map of L1495 with nonphysical values of $f_d < 1$. To estimate f_d, we use only well-defined column densities, with $N(C^{18}O)/\Delta N(C^{18}O) > 5$.

The resulting distributions of depletion factors across the entire L1495 map obtained for different reference abundances of CO are presented in Figure 2. The chosen reference fractional abundances affect the CO depletion factor, with the highest $X_{ref}(CO)$ giving the largest f_d and the widest range of f_d (see Table 4). Taking into account the uncertainties of the calculated $C^{18}O$ column densities (including the LTE assumption, which results in underestimation of the column density), the first two reference abundances give

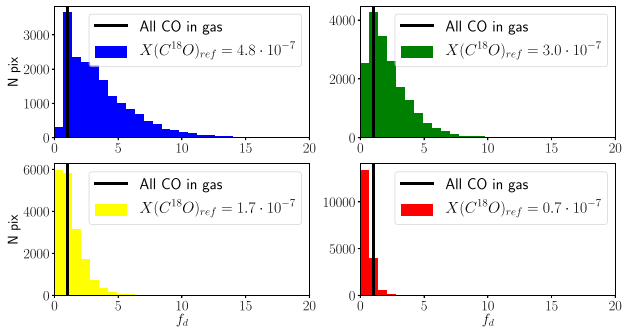

Figure 2. CO depletion f_d measured across all B7, B10, B211, B213 and B218 regions, mapped by Tafalla & Hacar (2015), using various reference CO abundances. The black vertical line shows $f_d = 1$, when all CO is in the gas phase. Maps of the CO depletion factor, obtained with $X_{ref}(C^{18}O) = 4.8\times10^{-7}$, across the B7, B10, B211, B213, and B218 regions of L1495 are available in the .tar.gz package.

(The data used to create this figure are available.)

median f_d values in the cloud below 1, which is nonphysical. Toward the least depleted areas, we find $f_d \simeq 0.2$, 0.5, 0.9, and 1.5 with $X_{ref}(C^{18}O) = 0.7\times10^{-7}$, 1.7×10^{-7}, 3.0×10^{-7}, and 4.82×10^{-7}, respectively. The choice of the reference value was based on the one that gave the lowest number of points (out of the total 22,941) with $f_d < 1$.

Thus we use the highest reference abundance of CO equal to 2.7×10^{-4} with respect to (w.r.t.) H_2 (which gives 4.8×10^{-7} of $C^{18}O$ w.r.t. H_2), which gives only 7% of nonphysical f_d values across the maps, to measure CO depletion. These 7% may be caused by a large spread of this reference value (see Table 4 and Lacy et al. 1994). The number of nonphysical values is small, and we do not aim at fitting the best reference CO abundance; we just use one of the well established reference values that fits better.

3.2.3. $C^{18}O$ Abundance and CO Depletion Factor

The depletion factor of CO is generally moderate in L1495, ranging from 1 to 44 toward the studied cores (see Figures 3 and 4; there are just a few pixels with high f_d, so we limit the histogram in Figure 3 at $f_d = 25$ to show the dynamic range better). Among them, core 7 shows the lowest depletion factor, $f_d = 1–4$, as well as the entire B211 region with $f_d = 1–4$. Cores 10, 11, and 16 (B213 region) show very similar depletion values, 2–44, the highest in our data set (which confirms B213 being more dynamically evolved than B211 and B10), with a median of $f_d = 6–8$; there are high values for both starless and protostellar cores. Cores 1 and 6 of the B10 region show intermediate values

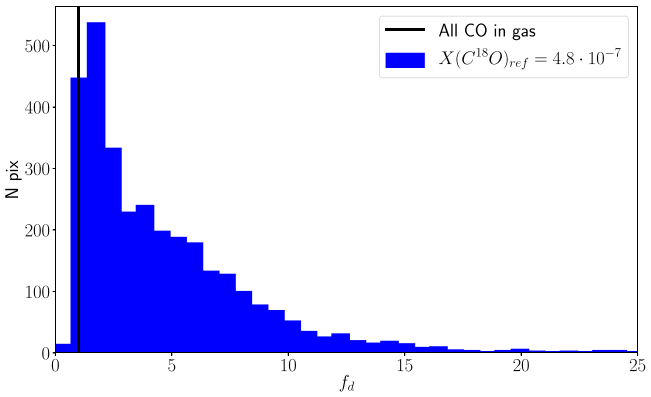

Figure 3. The distribution of CO depletion factor in the maps of all studied cores (except for core 35). The black vertical line represents $f_d = 1$ (all CO in the gas phase). Maps of CO depletion factor across the cores are available in the .tar.gz package. These maps can be used to recreate Figures 3, 4, 6–8, 10, and 11.

(The data used to create this figure are available.)

of $f_d = 1$–14. Given the angular resolution of Herschel maps, these numbers could be lower limits of f_d. CO depletion toward core 35 was not measured since there are no available CO maps for this region.

3.3. Methanol Distribution

Figure 5 shows the distribution of integrated intensity over all observed methanol lines and contours of the dust continuum emission mapped with Herschel/SPIRE (Palmeirim et al. 2013) toward all seven observed cores. The gas-phase methanol is expected to be most abundant in the areas where CO is actively freezing onto the dust grains, and the methanol production overcomes its freeze-out (see Vasyunin et al. 2017). We assume the lines are optically thin (see Section 3.4), so the methanol distribution can be traced by the intensity maps.

Toward three cores methanol appears in a shell around the densest area (cores 1, 7, and 10) where it is moderately (core 10) or significantly (cores 1 and 7) depleted. Toward two cores (6 and 16), methanol emission peaks are close to the dust emission peaks. Cores 11 and 35 show something in between: the methanol peaks are close to the dust emission peak, but the highest contour of methanol emission has an elongated arch-like shape and rather surrounds the highest dust emission contour. There are no CO observations for core 35.

The methanol emission in the methanol-rich shells around cores 1, 7, 10, 11, and 35 is not uniform, with one or two spots of enhanced methanol toward each core. Such methanol distribution (in a shell around the dense parts with one or two emission peaks within the shell) was observed before toward other dense cores in Taurus (L1498, L1544, L1521E; Tafalla et al. 2006; Bizzocchi et al. 2014; Nagy et al. 2019) and Ophiuchus (Oph-H-MM1; Harju et al. 2020). We confirm that a shell-like methanol distribution is also widespread in the dense cores of the L1495 filament.

3.4. Methanol Column Densities

We measure the methanol column densities via the rotational diagrams based on the four brightest lines detected across all cores. We use only the pixels with all four lines detected with $S/N > 5$. We assume that the methanol lines are optically thin (as is shown in Scibelli & Shirley 2020), consistent with LTE, and the fractional abundance of A- and E-methanol is 1:1. We calculate the column density of the upper level population, N_{up}, as

$$N_{up} = \frac{8\pi k W \nu^2}{Ahc^3}, \quad (4)$$

where k is the Boltzmann constant, W is the integrated intensity of the line, ν is the frequency, A is the Einstein coefficient (given in Table 2), h is the Planck constant, and c is the speed of light (e.g., Goldsmith & Langer 1999).

We fit a linear function $y = ax + b$ to the plot $\ln(N_{up}/g_{up})$ versus E_{up}/k, where g_{up} is the statistical weight of the upper level ($g_J = 2J + 1$, with J being the rotational quantum number) and E_{up} is the energy of the upper level. Then the rotational temperature is $T_{rot} = -1/a$, and the total column density is $N_{tot} = e^b Q_{rot}$, where Q_{rot} is the rotational partition function. For an asymmetric rotor (such as methanol) the partition function can be approximated as

$$Q_{rot} = \frac{5.34 \times 10^6}{\sigma} \sqrt{\frac{T_{rot}^3}{ABC}}, \quad (5)$$

where $\sigma = 1$ is a symmetry number, A, B, and C are the rotational constants (in MHz, taken from JPL; Pickett et al. 1998); for details see Gordy & Cook (1970). The uncertainty of the column density was calculated via propagation of errors of the b coefficient. After measuring T_{rot} and N_{tot} we exclude all data points with relative uncertainties higher than 1/3 from our analysis.

The rotational temperature of methanol varies in the range 6–16 K, with a typical uncertainty of 5%–10% (see Figure 14 for the T_{rot} and ΔT_{rot} distributions and Figure 16 for the T_{rot} maps). The median $T_{rot} = 9.1$ K is consistent with the gas temperatures of the cores (8–10 K) measured with ammonia by Seo et al. (2015), which also supports our assumption of LTE.

The total methanol column density varies in the range $(0.5–7.0) \times 10^{13}$ cm^{-2} across all cores with a typical uncertainty of 10%–20% (see Figure 15). Our column densities measured with the rotational diagrams are consistent with those measured with RADEX by Scibelli & Shirley (2020) toward the ammonia peaks. Figure 17 shows the column density maps. Since the brightest methanol emission avoids the dense core centers, we register higher values of column density (up to 7×10^{13} cm^{-2}) than Scibelli & Shirley (2020) did (up to 3.5×10^{13} cm^{-2}), as they pointed only toward the ammonia peaks.

Since we assume the lines are optically thin, the distribution of column density is similar to the distribution of the integrated intensity (see Figure 17, although toward cores 11 and 16 we have only a few points detected with $S/N > 5$ in all four lines).

3.5. Methanol Abundance

We use the $N(H_2)$ obtained by fitting the spectral energy distribution (SED) to the Herschel data to measure the methanol abundance. Methanol abundance maps are shown in Figure 6. We obtain methanol abundances of $(0.5–8.5) \times 10^{-9}$ with a median value of 1.9×10^{-9} (see median column densities, rotational temperature, and abundance of methanol toward individual cores in Table 5). Cores 1, 6, 7, and 35, which belong to the less evolved regions B10, B211, and B216,

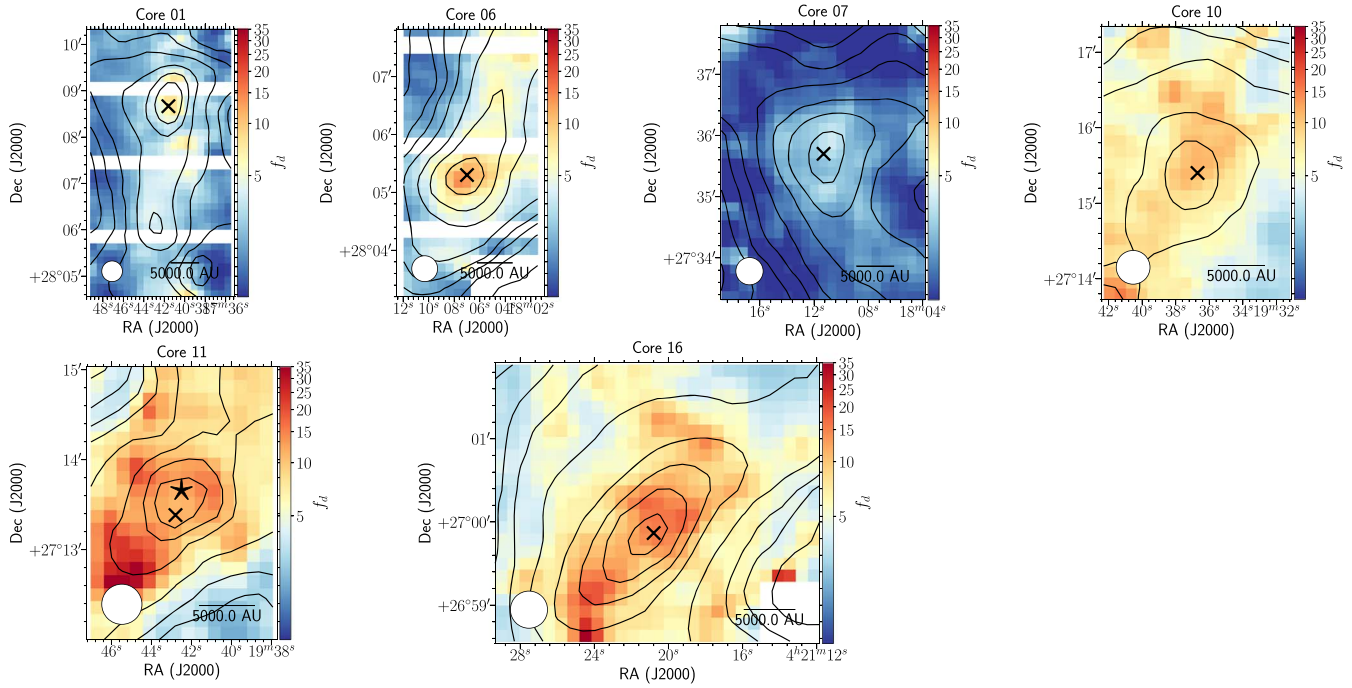

Figure 4. Maps of CO depletion factor (color scale) toward the observed cores based on $C^{18}O$ observations from Tafalla & Hacar (2015). Black contours show visual extinction at $A_V = 3$, 4, 5, 6, 8, 12, 16, 20, and 24 mag. The top A_V contours are at $A_V = 24$ mag for core 16 and at $A_V = 20$ mag for the other cores. The black star shows the position of Class 0 protostar IRAS 04166+2706 (Santiago-García et al. 2009); crosses show the Herschel/SPIRE dust emission peaks. The white circle at the bottom left of each map shows the 23″ beam. The white strips in the maps of cores 1 and 6 originate from the NaNs in the B10 map available at CDS. Maps of the visual extinction across the cores are available in the .tar.gz package. These maps can be used to recreate Figures 4–8, 10, 11, and 16–18.

(The data used to create this figure are available.)

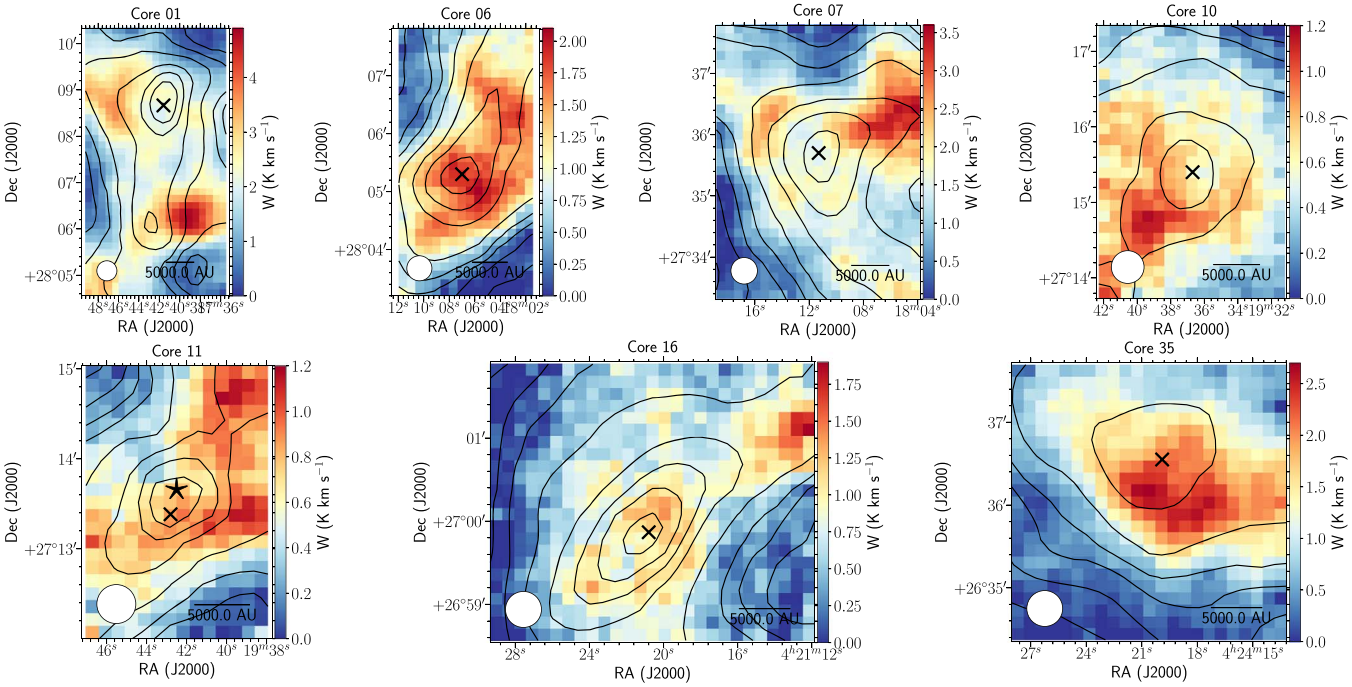

Figure 5. Integrated intensity of all observed methanol lines toward the observed cores (color scale) and visual extinction (black contours at $A_V = 3$, 4, 5, 6, 8, 12, 16, 20, and 24 mag). The top A_V contours are at $A_V = 24$ mag for core 16 and at $A_V = 20$ mag for the other cores. The black star shows the position of Class 0 protostar IRAS 04166+2706 (Santiago-García et al. 2009); crosses show the Herschel/SPIRE dust emission peaks. The white circle at the bottom left of each map shows the 26″ IRAM beam.

show higher methanol abundance than cores 10, 11, and 16 from the more evolved B213 region, by a factor of two. The highest methanol abundance (8.5×10^{-9}) is observed toward a local methanol peak in a shell around core 1. In all cores, the highest methanol abundance is observed in the shells around the cores, with $A_V = 5$–10 mag (see the left panel of Figure 7)

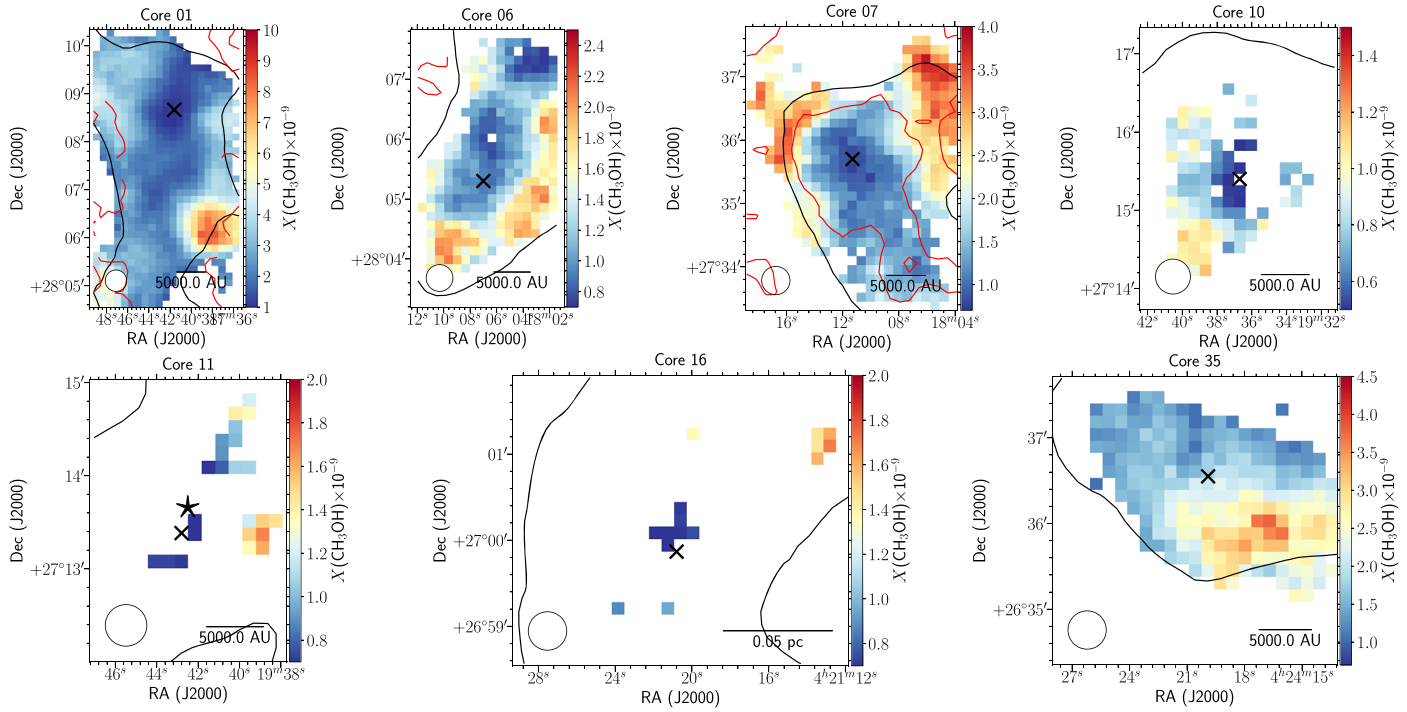

Figure 6. Methanol abundance maps. The red contours show $f_d = 1.6$ and the black contours show $A_V = 6$ mag, the values of observed CO depletion and visual extinction associated with the highest methanol abundance. Maps of methanol abundances are available in the .tar.gz package. These maps can be used to recreate Figures 6–8, 10, and 11.

(The data used to create this figure are available.)

Table 5
Median Column Densities, Rotational Temperatures, and Abundances of Methanol for Each Core, and the Cores' Chemical Ages Derived from the Chemical Model

Core	$N(CH_3OH)$ (10^{13} cm^{-2})	T_{rot} (K)	$X(CH_3OH)$ $\times10^{-9}$	f_d	Age (kyr)
1	2.81	9.3	2.68	8	118
6	1.83	8.2	1.28	14	226
7	2.23	8.9	1.76	4	89
10	1.18	9.0	0.84	12	433
11	1.39	10.9	1.07	44	1000
16	1.70	8.6	0.88	17	248
35	2.24	9.2	1.89	4[a]	187

Note. The age estimates are based on the highest observed CO depletion factors.

[a] We have no CO data for core 35, so we adapt the lowest f_d observed toward our cores ($f_d = 4$ for core 7), since the region B216 is supposed to be young (Hacar et al. 2013; Seo et al. 2015).

and $f_d = 1.5$–2.0 (see the right panel of Figure 8), and correlates with gaseous CO abundance (see the left panel of Figure 8). The CO depletion factor increases with visual extinction (see the right panel of Figure 7); however, there is a general trend rather than a single correlation: f_d always increases with A_V within one core (see the plots of individual cores in Figure 11). Sometimes the emission has a prominent peak of enhanced abundance (cores 1 and 35), on average associated with $A_V \simeq 6$ mag and $f_d \simeq 1.6$, which is well illustrated by the abundance maps of cores 1 and 7 in Figure 6. For cores 10, 11, and 16 we do not have enough data points to test whether the average rule applies to them. In all cores methanol is significantly depleted toward the dust peaks where the observed abundance is minimal (except for core 35 where minimal abundance is observed to the north of the dust peak).

In L1544 and Oph-H-MM1 the lopsided distribution of methanol in the shell was explained by the UV irradiation of one side and shielding of the other side of the cores (Spezzano et al. 2016; Harju et al. 2020) and the probable presence of a slow shock (Punanova et al. 2018b; Harju et al. 2020). In L1495, there are no preferred UV irradiation directions or areas shielded more than others (the background column densities on either side of the filament differ by a factor of 2; Palmeirim et al. 2013). Although illumination of the cores could locally be nonuniform: there are protostars of various classes in and around the filament. Besides that, from Hacar et al. (2013) we know that the cores reside in the dense "fertile" fibers next to less dense "sterile" fibers; those overlap along the line of sight and probably both shield methanol from UV destruction and contribute to the observed methanol abundance, producing local abundance peaks like the ones toward cores 1 and 35. Yet there is no evidence of slow shocks in the L1495 cores: the local velocity gradients of the shells traced by the HCO^+ emission show homogeneous patterns (Punanova et al. 2018a), except for the protostellar core 11.

4. Modeling Chemical Composition of the Filament Cores

4.1. Physical Models of the Cores

For the purpose of modeling, we assumed that the cores are spherically symmetric. Under this assumption, we derived temperature and density profiles of the cores. First, we used simple polynomial fits to the radial distributions of Herschel

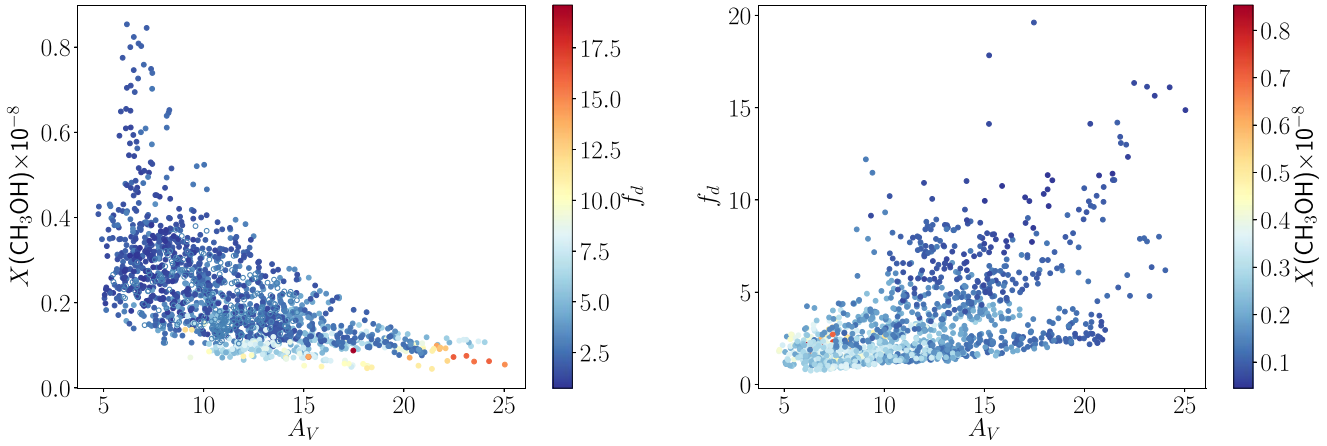

Figure 7. Left: the observed abundance of CH_3OH for all of the pixels in all of the maps combined as a function of line-of-sight visual extinction; the color scale represents the CO depletion factor. Right: the CO depletion factor as a function of line-of-sight visual extinction; the color scale represents the methanol abundance.

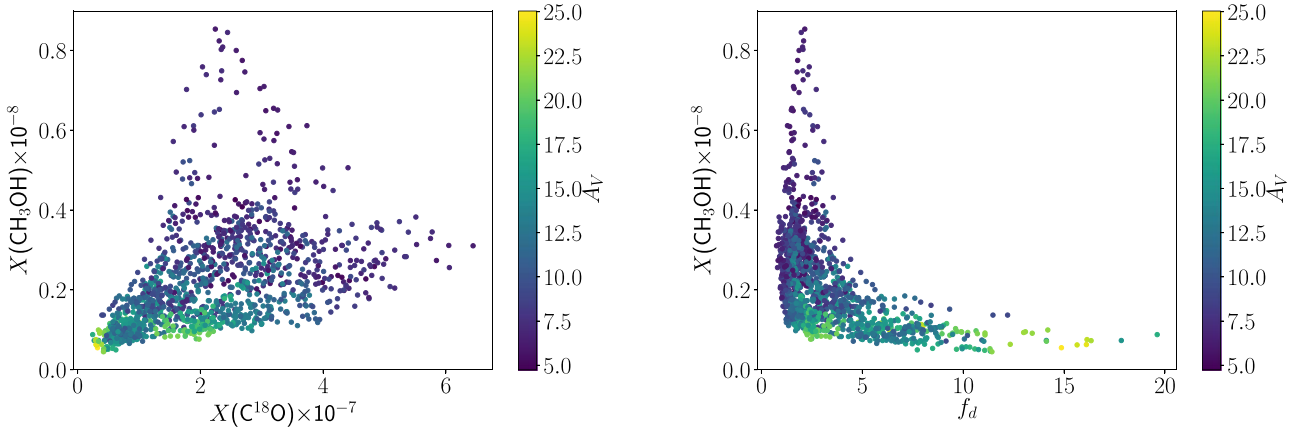

Figure 8. The observed abundance of CH_3OH for all of the pixels in all of the maps combined as a function of observed abundance of $C^{18}O$ (left) and CO depletion factor (right). The color scale represents the line-of-sight visual extinction.

molecular column density ($N(H_2)$). Then, we converted the molecular hydrogen column density to volume density. A similar approach was recently published in Hasenberger & Alves (2020). Two key assumptions in this procedure are (i) the cores are spherical and (ii) the cores can be divided into "onion shells" of constant gas density and the same thickness. We also assume that the model center coincides with the observed dust peak. The derived H_2 volume densities have been tested to provide the original H_2 column densities when using the reverse procedure of obtaining column densities from volume densities described in Jiménez-Serra et al. (2016). The physical models of the cores are shown in Figure 9. Gas temperature in the cores was assumed equal to the dust temperature derived from Herschel data. This assumption is reasonable for our study, as we are focused on chemistry. The majority of chemical processes in the gas phase exhibit weak dependence on gas temperature. For example, rates of ion–molecule reactions that are believed to dominate low-temperature gas-phase chemistry depend on temperature as $\sqrt{T_{\rm gas}}$. In contrast, rates of chemical processes on surfaces of interstellar grains such as thermal desorption or thermal hopping of adsorbed species typically show exponential dependence on temperature. Moreover, at gas densities above 10^4 cm^{-3} gas and dust are close to thermal coupling (Goldsmith 2001). Finally, the L1495 filament does not possess signs of violent processes such as shock waves that may heat the gas to very high temperatures (e.g., Tafalla & Hacar 2015). Thus, we believe that our assumption on equality of gas and dust temperatures is justified.

4.2. Chemical Model

In this work, we utilize the MONACO chemical model previously described in Vasyunin et al. (2017) with several minor updates described in Nagy et al. (2019) and Scibelli et al. (2021). This is a "three-phase" chemical model capable of simulating chemical evolution in the gas phase, on surfaces of icy mantles of interstellar dust grains, and in the bulk of icy mantles. MONACO is a 0D time-dependent chemical model based on rate equations. In order to simulate chemistry in prestellar cores, the chemical code is wrapped into a 1D static physical models that includes radial distributions of the most important physical parameters that control chemistry in a prestellar core: gas density, gas and dust temperatures, and visual extinction (see Section 4.1). With the model, time-dependent fractional abundances calculated with the MONACO code at each radial point of the 1D model can be converted to column densities of species, thus allowing direct comparison with observational data.

Since dense cores considered in this work are located in a filament of molecular gas, we use a two-step approach to model their chemical evolution. In the first step, chemistry in a low-density translucent medium is simulated ($n_{\rm H} = 10^2$ cm^{-3},

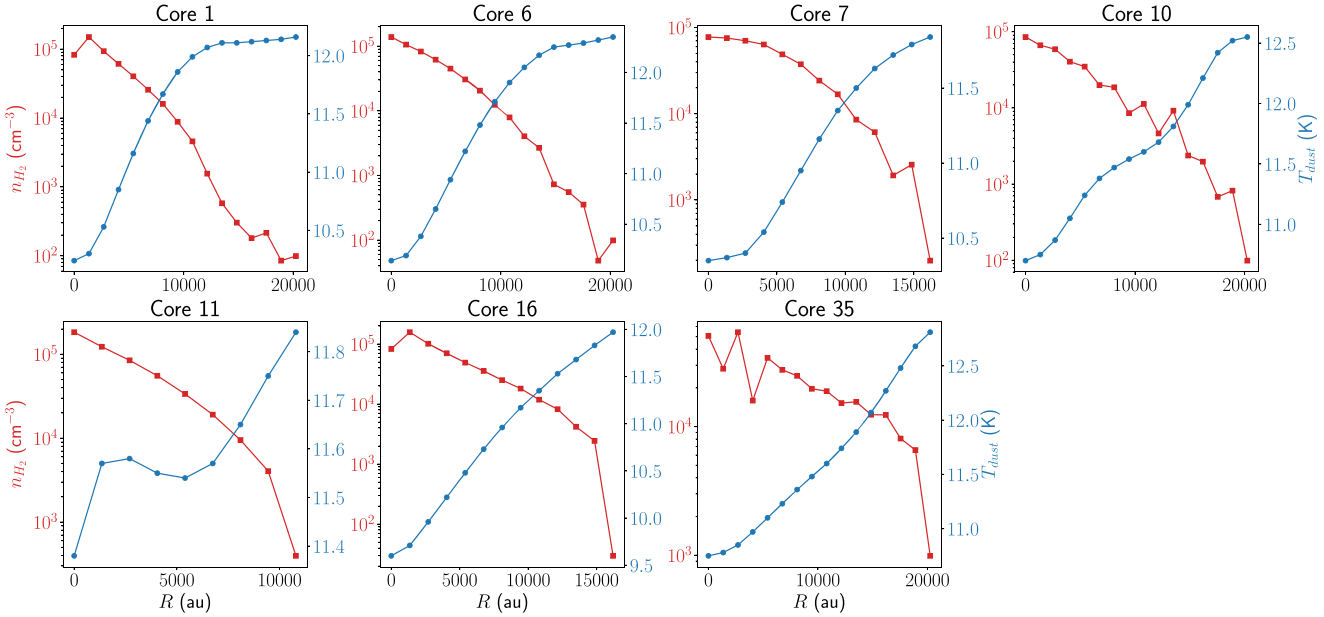

Figure 9. Physical models of the cores: molecular hydrogen number density (red) and dust temperature (blue). The data behind this figure are available in machine-readable format.

(The data used to create this figure are available.)

$T_{\rm gas} = T_{\rm dust} = 20$ K, $A_V = 2$ mag) over a period of 10^6 yr. The initial chemical composition of the medium corresponds to elemental abundances 1 (EA1) from Table 1 in Wakelam & Herbst (2008). In the second step, chemical evolution in the core is simulated using the abundances of chemical species at the final moment of time of step one as the initial chemical composition.

Other key parameters of the chemical model are the following. The cosmic-ray ionization rate is taken equal to the standard value of 1.3×10^{-17} s^{-1}. The dust grain radius in the model is 10^{-5} cm. Four upper layers of multilayered grain mantle are considered as belonging to the surface in accordance with Vasyunin & Herbst (2013b). The sticking probability for all species is unity (e.g., Fraser & van Dishoeck 2004; Chaabouni et al. 2012, and references therein). Surface species can be delivered to the gas phase via thermal desorption, photodesorption, cosmic-ray-induced desorption (Hasegawa & Herbst 1993), and reactive desorption.

The photodesorption yield for CO was measured in a number of laboratory experiments. It was found to be high, temperature- and wavelength-dependent, and of the order of 0.001–0.1 molecules per incident photon (e.g., Öberg et al. 2009; Fayolle et al. 2011; Chen et al. 2014; Muñoz Caro et al. 2016; Paardekooper et al. 2016). We tested various CO photodesorption yields (0.001–0.1) applied to our four models and found that a high CO photodesorption yield, 0.03 molecules per incident photon and above, significantly affects the process of CO depletion in the models of prestellar cores considered in this study. For two cores, observed CO depletion factors were either never reached in the model (core 11), or were reached on timescales $>10^6$ yr (core 10). Such a timescale is much longer than typical estimates of the "chemical age" of prestellar cores, which is very uncertain, but in most studies is well below 10^6 yr: (1–3) $\times 10^5$ yr (e.g., Tafalla & Santiago 2004; Walsh et al. 2009; Jiménez-Serra et al. 2016, 2021; Nagy et al. 2019; Lattanzi et al. 2020; Scibelli et al. 2021), sometimes up to (3–7) $\times 10^5$ yr (e.g., Loison et al. 2020). Thus, with certain simplification, in this study we employed a constant photodesorption yield for CO equal to 10^{-2} molecules per incident photon, following Fayolle et al. (2011), where this value was obtained for the UV field in prestellar cores in accurate experiments with tunable synchrotron radiation. For methanol, following Bertin et al. (2016) and Cruz-Diaz et al. (2016), we employed a photodesorption yield equal to 10^{-5} molecules per incident photon. This yield was also assumed for other species in the model.

The efficiency of reactive desorption, i.e., the probability of a product of an exothermic surface reaction being ejected to the gas phase upon formation, depends on the particular reaction, product, and type of surface in a complex and still poorly studied way (see, e.g., Garrod et al. 2007; Vasyunin & Herbst 2013a; Minissale et al. 2016; Chuang et al. 2018). Next, the rate of reactive desorption depends on the rate of related surface reactions. Rates of surface diffusive reactions of hydrogenation are mainly controlled by diffusion of atomic hydrogen. The rates of diffusion, in turn, are poorly known. Reactive desorption is believed to be the key process that delivers methanol, formed on cold grains during CO hydrogenation, to the gas phase (Garrod et al. 2006). Given that there are no known efficient gas-phase routes of methanol formation (Geppert et al. 2006), it is tempting to utilize the extensive observational data set on CO and CH_3OH presented in this study to constrain model parameters related to the formation and desorption of methanol in the conditions of cold dense cores. Thus, we consider four parameterizations of reactive desorption and surface mobility of hydrogen atoms: (i) tunneling for hydrogen diffusion enabled, and treatment of reactive desorption following Minissale et al. (2016) with parameters as in Vasyunin et al. (2017) (rdMD); (ii) no tunneling for hydrogen diffusion, only thermal hopping, and diffusion/desorption energy ratio is 0.5, rdMD; (iii) tunneling for hydrogen diffusion, single reactive desorption probability of

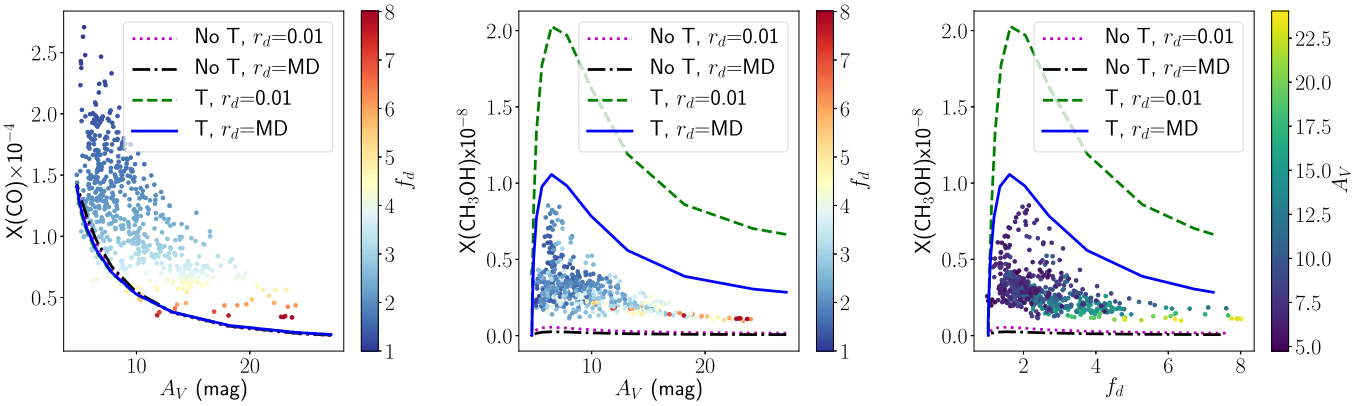

Figure 10. The comparison of the observed (colored dots) and modeled CO abundance profiles as a function of visual extinction (left); CH_3OH abundance profiles as a function of visual extinction (middle); and CO depletion factor (right) for core 1. The color scale represents CO depletion factor f_d (left and middle) and visual extinction A_V (right) in the individual pixels. The models include: no tunneling for diffusion of H and H_2 and 1% reactive desorption efficiency (dotted magenta line); no tunneling and reactive desorption efficiency from Minissale et al. (2016) (dashed-dotted black line); tunneling and 1% reactive desorption efficiency (dashed green line); tunneling and reactive desorption efficiency from Minissale et al. (2016) (solid blue line).

1% (rd1); (iv) no tunneling for hydrogen diffusion, rd1. Those four particular models were chosen based on the fact that the efficiency of quantum tunneling for atomic diffusion on grains is still debated (e.g., Rimola et al. 2014; Lamberts & Kästner 2017). For these parameterizations of reactive desorption, we aim to check the feasibility of approaches utilized in our previous works (e.g., Vasyunin & Herbst 2013a; Vasyunin et al. 2017), as well in a number of other studies (e.g., Garrod et al. 2007; Ruaud et al. 2016; Jin & Garrod 2020).

4.3. Observed and Modeled Abundances

Using the parameters described above, we performed 1D chemical modeling of all dense cores in the L1495 filament considered in this study. To estimate the chemical age of the cores, we used the highest values of depletion factor reached in each core (see Table 5). Modeled radial profiles of CO and CH_3OH column densities and fractional abundances were then compared with the observed values. The four models produce almost the same CO abundance (see left panel of Figure 10), while methanol abundance differs significantly from model to model (see central and right panels of Figure 10). Although none of the models matches the observations perfectly, the model with quantum tunneling for diffusion of atomic hydrogen and treatment of reactive desorption according to parameterization by Minissale et al. (2016) produces results with the closest agreement to the observed data, as shown in Figure 10 with an example of core 1. The left panels of Figure 11 show the comparison of the observed CO abundances versus visual extinction and the results of all four chemical models.

The best model reproduces the observed CO abundances very well with a slight (by a factor of a few) underestimation likely due to the fact that we see the CO emission from the cloud surrounding the cores. The other models (with higher reactive desorption and no tunneling) produce the same amount of CO (see left panels of Figures 10 and 11). This result shows that the cores are close to spherical shape, and our assumption used to convert gas column density to volume density is applicable for our cores.

In the middle panels of Figure 11, observed and modeled abundances of methanol are presented. One can see that CH_3OH abundances obtained with the best-fit model are overestimated by a factor of a few in all cores, similar to what was seen before in the models (like in L1521E in Scibelli et al. 2021), except core 11. In that core, the model matches the observed values well. However, the number of data points for core 11 is small. Another reason for the mismatch might be our assumption of the A:E methanol ratio of 1:1. If we treat the two forms separately as is shown in Section 3.4, E-methanol shows higher column densities than A-methanol, although with large uncertainties. On the other hand, Harju et al. (2020) present the ratio A:E = 1.3. The complex correlation between methanol abundance and visual extinction is clearly seen in both the model and observations, as illustrated in Figure 18: we detect the lowest methanol column densities in the outskirts of the cores; they rapidly increase with A_V up to the line-of-sight $A_V \sim 8$, and then decrease with A_V.

In the right panels of Figure 11, abundances of methanol versus depletion factor f_d are presented. Interestingly, the maximum abundances of CH_3OH correspond to moderate values of CO depletion factor, f_d = 1.5–2, which is associated with volume densities of $\sim 10^4$ cm^{-3} and temperature of ~11.5 K. This fact supports the scenario of formation of methanol during the onset of catastrophic CO freeze-out in prestellar cores (Bizzocchi et al. 2014; Vasyunin et al. 2017). The almost linear correlation between the CH_3OH and CO abundances shown in the left panel of Figure 8 might be related to the efficiency of CO hydrogenation to methanol on grains, as was suggested by Harju et al. (2020).

Figures 10 and 11 show that models without tunneling for hydrogen diffusion severely underproduce methanol abundances, while the model with tunneling and 1% probability of reactive desorption, same for all species, overproduces the abundance of methanol by more than one order of magnitude in the majority of the cores. The only exception is core 7, where methanol abundance is better reproduced by the model without tunneling and 1% probability of reactive desorption. This is the core with the lowest CO depletion factor (f_d = 4) in this study. A low f_d value can be attributed to the very young chemical age of the core (e.g., L1521E, Nagy et al. 2019; Scibelli et al. 2021). For such a young core, our modeling approach based on a static density profile and "low metals" elemental chemical composition is most likely less accurate than for other, more evolved cores considered

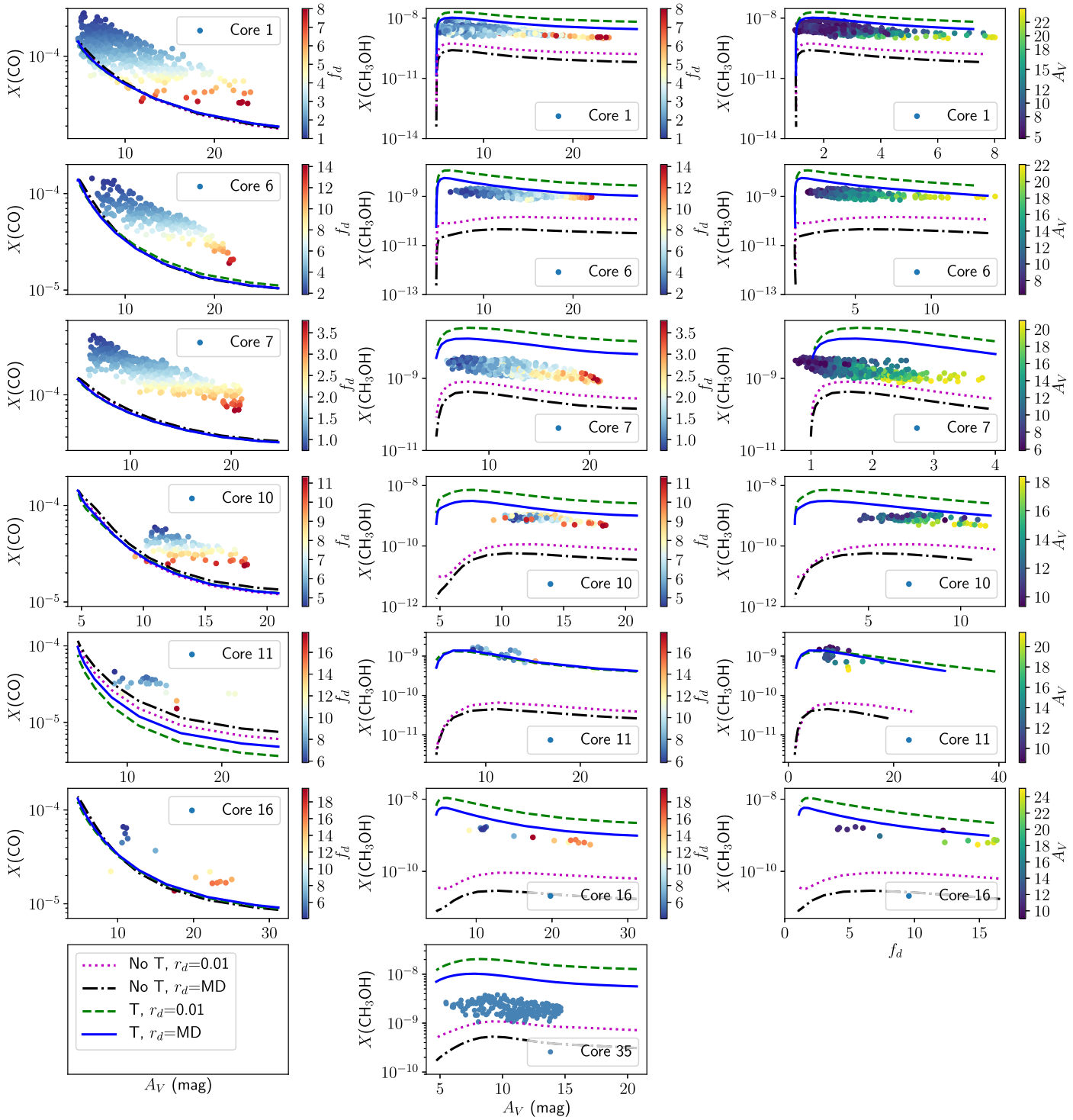

Figure 11. The comparison of the observed (colored dots) and modeled CO abundance profiles as a function of visual extinction (left); CH_3OH abundance profiles as a function of visual extinction (middle); and CO depletion factor (right) for all cores. The color scale represents CO depletion factor f_d (left and middle) and visual extinction A_V (right) in the individual pixels. The data points of core 35 are all shown with the same color since there are no CO data for this core. The models include: no tunneling for diffusion of H and H_2 and 1% reactive desorption efficiency (dotted magenta line); no tunneling and reactive desorption efficiency from Minissale et al. (2016) (dashed-dotted black line); tunneling and 1% reactive desorption efficiency (dashed green line); tunneling and reactive desorption efficiency from Minissale et al. (2016) (solid blue line). The model curves behind this figure are available in machine-readable format.

(The data used to create this figure are available.)

in this study. To summarize, observational data on CO and CH_3OH in the dense cores of the L1495 filament can be fitted best with the MONACO code when tunneling for atomic hydrogen is enabled, and reactive desorption is treated following the approach by Minissale et al. (2016).

5. Discussion

In this work, we present an extensive observational study of methanol distribution in dense cores within the L1495 filament. The wealth of observational data is analyzed statistically, and

studied with a sophisticated numerical gas–grain model of chemical evolution in star-forming regions. Modeling results, especially the spatial distribution of species, agree surprisingly well with observational data given the simplicity of the physical models adopted to represent dense cores in this study. The cores are approximated as static spherical objects with density and temperature gradients. While such an approximation is often considered too simplistic, it appears to be sufficiently accurate for modeling of the distribution of chemical species in dense cores. This fact may suggest that dense prestellar cores do not significantly deviate from spherical symmetry and evolve dynamically on timescales longer than the timescales of chemical evolution. Characteristic timescales of chemical evolution in cores of average volume density of 10^5 cm^{-3} are of the order of 10^5 yr, close to freefall times for starless cores with similar average volume densities (see, e.g., Kirk et al. 2005; Tafalla et al. 2006; André et al. 2014). However, even the most dynamically evolved prestellar core (L1544) has been found to contract at a much slower rate than freefall (Keto & Caselli 2010), probably due to the retarding action of magnetic fields. Therefore, chemistry indeed proceeds faster than dynamical evolution at core scales.

The extensive set of observational data allowed us to put constraints on the treatment of reactive desorption, at least for the astrochemical model that includes only diffusive surface chemistry. The observed abundances of methanol in the gas phase of prestellar cores can be reproduced most accurately with the model that includes quantum tunneling for diffusion of atomic hydrogen on surfaces of grains and parameterization of probabilities of reactive desorption following Minissale et al. (2016). A model with those assumptions is presented in Jiménez-Serra et al. (2016) and Vasyunin et al. (2017). The model successfully reproduced the abundances of many molecules including COMs in L1544 and several other cores (e.g., Nagy et al. 2019; Lattanzi et al. 2020; Jiménez-Serra et al. 2021). On the other hand, in the case of the very young core L1521E the model overpredicted methanol abundance and underpredicted the abundances of COMs (Scibelli et al. 2021).

In Vasyunin et al. (2017), the maximum abundance of methanol in the L1544 prestellar core is located near local $A_V = 4$ mag (that is $A_V \sim 8$ on the line of sight). This value is similar for other cores. It corresponds to the location in spherical clouds where catastrophic freeze-out of CO molecules starts. The onset of such catastrophic CO freeze-out corresponds to the highest accretion rate of carbon monoxide onto grains, thus facilitating the most efficient methanol formation across the core. Analysis of observations presented in this study confirms that methanol abundances reach their maxima in different cores at similar values of visual extinction. Moreover, the locations of CH_3OH abundance maxima typically correspond to moderate values of CO depletion factor, $f_d \simeq 2$. Thus, earlier conclusions on the methanol formation scenario based on limited observational data are now confirmed on a more significant data set.

Although this study advocates for tunneling as a source of mobility of hydrogen atoms and molecules on grains, one has to bear in mind that the model utilized in this work includes only diffusive surface chemistry. Tunneling increases the pace of CO hydrogenation into formaldehyde and methanol. However, the conclusion may change if chemical models that include nondiffusive grain chemistry are applied to the presented data. One can speculate about very fast nondiffusive mechanisms of formation of those two species that may render diffusive tunneling less important (such as recombination of various CH_nO radicals produced in close proximity to each other on the icy grain surface, Fedoseev et al. 2015; Jin & Garrod 2020). On the other hand, one must bear in mind that the CO hydrogenation sequence may include efficient H_2 abstraction reactions. Those reactions may reduce the rate of H_2CO and CH_3OH formation. In any case, statistical data on CO and CH_3OH abundances and their spatial distribution in cold cores of the L1495 filament provide a unique tool to test current and future gas–grain chemical models.

Chemistry in dense cores and clumps is normally modeled with the so-called low-metal abundances (e.g., Hasegawa et al. 1992; Lee et al. 1998; Sipilä et al. 2020) summarized in Wakelam & Herbst (2008) following Graedel et al. (1982). While the low- and high-metal abundances are supposed to represent the abundances of such heavy elements as Fe, Mg, Si, S, etc., CNO elements also have different abundances in these two sets. Graedel et al. (1982) note that poorly constrained metal abundances correlate with (and influence) electron fraction; high-metal abundance corresponds to $x(e^-) >$ few $\times$ 10^{-7} at $n \simeq 10^4$–10^5 cm^{-3}. They also note that the relative abundances change with age: in particular, between 10^5 and 10^7 yr (the typical chemical age of a prestellar core is (1–3) $\times$ 10^5 yr) the abundances may change by an order of magnitude. Caselli et al. (1998) showed that the electron fraction depends on carbon and oxygen elemental depletion; they find $x(e^-) \simeq 2.5 \times 10^{-7}$ for L1495 (with an assumption of high elemental depletion), which is similar to our estimation $x(e^-) \sim 2 \times 10^{-7}$ based on DCO^+ and $H^{13}CO^+$ observations (A. Punanova et al. 2022, in preparation). Another argument against standard "low metals" elemental abundances appeared in the course of this study. The best-fit reference undepleted abundance of CO for L1495 confirmed by this work is 2.7×10^{-4} w.r.t. H_2. This implies elemental abundances of both carbon and oxygen available for gas-phase chemistry to be at least as high as that value. At the same time, "low metals" values for C and O abundances are 1.46×10^{-4} and 3.52×10^{-4} w.r.t. H_2, correspondingly (Wakelam & Herbst 2008), while "high metals" elemental abundances of C and O listed in that paper are 2.4×10^{-4} and 5.12×10^{-4} w.r.t. H_2.These considerations allow us at least to put in question the use of the low-metal abundances and suppose that probably high-metal abundances are more suitable for modeling dense cores in Taurus, as long as freeze-out is taken into account. Note, however, that direct application of "high metals" initial abundances leads to overestimation of abundances of sulfur-bearing species in models (Shalabiea 2001), unless S is heavily depleted onto dust grains (Caselli et al. 1994). Besides, Scibelli et al. (2021) showed that elevated sulfur abundance, needed to reproduce the abundances of S-bearing species (as also done by Seo et al. 2019), leads to a decrease in the abundances of COMs (e.g., CH_3OCH_3). On the other hand, the value of elemental sulfur abundance may deserve additional consideration, since understanding of sulfur chemistry is currently actively developing and still far from maturity (Laas & Caselli 2019; Nagy et al. 2019; Shingledecker et al. 2020, Cazaux et al. 2022).

6. Conclusions

In this paper we study the spatial distribution of methanol in cold dense cores. We explore correlations between the methanol

abundance and visual extinction and CO depletion. We test the three-phase chemical model MONACO (Vasyunin et al. 2017) against a large and homogeneous data set of 3 mm and 2 mm maps of methanol emission toward seven cold dense cores embedded in the L1495 filament. We vary key chemical model parameters to find the best match between the model and observational results. Our main findings are presented below.

1. The highest methanol intensity is observed both toward shells around the dust peaks of the cores (1, 7, 10) and toward the dust peaks (cores 6, 11, 16, 35). The column densities vary from 0.5×10^{13} to 7×10^{13} cm^{-2}.
2. The highest methanol gas abundance is observed in the shells around the cores (this is also true for those cores that have the CH_3OH peak located at the dust peak), while toward the dust peaks methanol is depleted. We obtain the methanol abundances of $(0.5–8.5) \times 10^{-9}$ with a median value of 1.9×10^{-9}.
3. We analyze CO gas abundance in the entire filament based on the $C^{18}O$ data from Tafalla & Hacar (2015) and conclude that the most suitable total undepleted CO abundance for the L1495 filament is 2.7×10^{-4} (Lacy et al. 1994). We find a CO depletion factor within the cores from 1 to 44, with the highest depletion factor toward the dust peaks from 4 to 44.
4. As expected, methanol abundance increases with visual extinction at low A_V, and reaches maximum values around line-of-sight $A_V \simeq 5–8$ mag and decreases at higher A_V.
5. The highest methanol abundance is observed around moderate values of $f_d \simeq 1.5–2$. This fact favors the scenario of methanol formation during the catastrophic freeze-out stage in starless cores.
6. Dense cores take various shapes; even in the plane of the sky the cores are far from circular. However, for simplicity, we use radial gradients of temperature and volume density as a base for the chemical model, and the modeled abundances reproduce well the observed ones, which implies that spherically symmetric models overall provide a good match to single-dish observations of dense cores.
7. We find that H and H_2 surface diffusion via tunneling is essential to reproduce the observed abundances of methanol. The model with disabled tunneling underproduces methanol abundance by 1.5 orders of magnitude.
8. We compared the models with flat 1% effectiveness of reactive desorption and the one calculated following the empirical formula yielded by Minissale et al. (2016). The model best reproduces methanol abundance with the Minissale et al. (2016) reactive desorption effectiveness, while flat 1% effectiveness tends to overproduce methanol abundance by a factor of a few.
9. Our observation results could serve as a benchmark for the forthcoming chemical models.

The authors thank the anonymous referee for valuable comments that helped to improve the manuscript. A.V. and A. P. are members of the Max Planck Partner Group at the Ural Federal University. A.P. and A.V. acknowledge the support of the Russian Science Foundation project 18-12-00351 and of the Russian Ministry of Science and Education via the State Assignment Contract no. FEUZ-2020-0038 (discussion on elemental abundances). The authors thank Vadim Krushinskiy for his help with Matplotlib and Gleb Fedoseev for discussion about photodesorption yield. S.S. is supported by National Science Foundation Graduate Research Fellowship (NSF GRF) Grant DGE-1143953.

Facilities: IRAM 30 m, Herschel

Software: astropy (Astropy Collaboration et al. 2013, 2018).

Appendix A
Column Density Calculation

We measure the methanol column densities via the rotational diagrams based on the four brightest lines detected across all cores (see Section 3.4). We use only the pixels with all four lines detected with signal-to-noise ratio $S/N > 5$. We assume the methanol lines are optically thin (as is shown in Scibelli & Shirley 2020), consistent with LTE, and the fractional abundance of *A*- and *E*-methanol is 1:1. We note that the *A*:*E* methanol ratio may differ from 1 (1.2–1.5 in the starless core H-MM1 in Ophiuchus and 1.3 in this filament, L1495, from RADEX modeling, Harju et al. 2017; Scibelli & Shirley 2020), while we use two *E*-lines and two *A*-lines for our rotational diagrams. To test the assumption of a 1:1 ratio, we took the data from the brightest pixels, where all six methanol lines observed in the project were well detected.

Figure 12 shows the rotational diagrams plotted for one position with the brightest methanol emission in core 1, based on two *A*-methanol lines (blue), four *E*-methanol lines (red), the four brightest methanol lines (used in the paper, black), and all six methanol lines (green). The resulting column densities and rotational temperatures are presented in Table 6. When we consider *A*- and *E*-methanol separately, the rotational diagrams give a lower rotational temperature, similar for both forms, 5.5–5.8 K (steeper slope of the diagrams), than that from the common rotational diagrams (9.5–10.1 K).

The total column density of *A*-methanol is lower than that of *E*-methanol, although the difference is within their large uncertainties. Previous works present the prevalence of *A*-methanol over *E*-methanol ($A{:}E = 1.3$ in Harju et al. 2020; Scibelli & Shirley 2020). The column densities based on the $A + E$ rotational diagrams are in agreement with those measured by Scibelli & Shirley (2020) with RADEX. The assumption of the $A{:}E = 1.3$ ratio would give even higher total column densities than those presented in this work. Given the small number of observed lines and the large uncertainties of the individual rotational diagrams, we decided to use both *A*- and *E*-methanol for the rotational diagrams. The difference between the results of the rotational diagrams based on four and six lines is negligible when error bars are taken into account, so we can rely on the four-points-based diagrams which we can plot in the majority of the pixels in our maps.

Table 6
Results of the Rotational Diagrams Based on Different Sets of the Methanol Lines

	CH_3OH-*A*	CH_3OH-*E*	$A + E$, 4 lines	$A + E$, 6 lines
N_{tot} (10^{13} cm^{-2})	4.6 ± 1.5	12.5 ± 6.3	6.6 ± 1.5	6.4 ± 1.3
T_{rot} (K)	5.8 ± 0.9	5.5 ± 0.9	10.1 ± 1.4	9.5 ± 1.2

Appendix B
Additional Figures

Here we present the comparison of $N(H_2)$ column density measured via Herschel dust continuum emission observations and via A_V infrared photometric measurements (Figure 13); the distribution of the methanol rotational temperatures (Figure 14); the distribution of the methanol column densities (Figure 15); the methanol rotational temperature maps (Figure 16); the methanol column density maps (Figure 17); and the correlation between the methanol column densities and visual extinction (Figure 18).

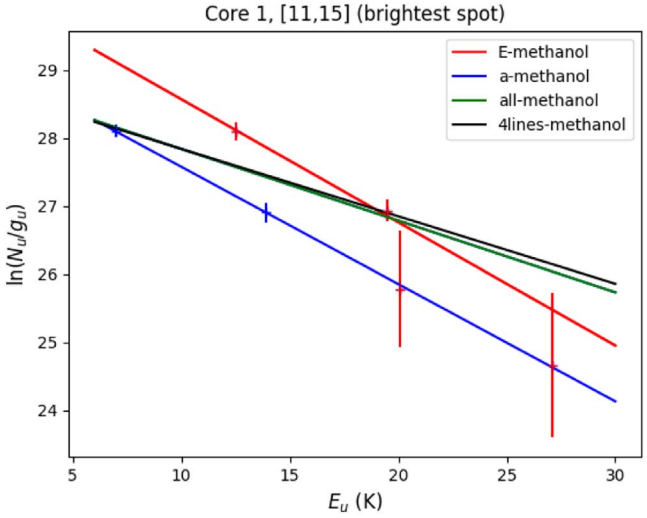

Figure 12. A comparison of methanol rotational diagrams toward the brightest pixel in core 1: based on *E*-methanol only (red line), based on *A*-methanol only (blue), based on all six *A*- and *E*-methanol lines including the weak higher energy lines (green), and based on the four *A*- and *E*-methanol lines (black, the one used to measure N_{tot}). Red symbols show *E*-methanol, blue symbols show *A*-methanol.

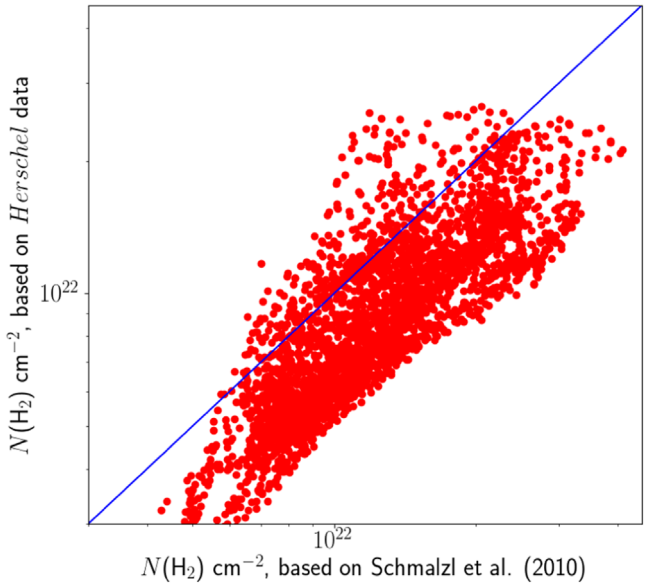

Figure 13. A comparison of $N(H_2)$ measured via Herschel dust continuum emission and via A_V measurements from infrared photometric observations (from Schmalzl et al. 2010). The solid blue line corresponds to 1:1 correlation.

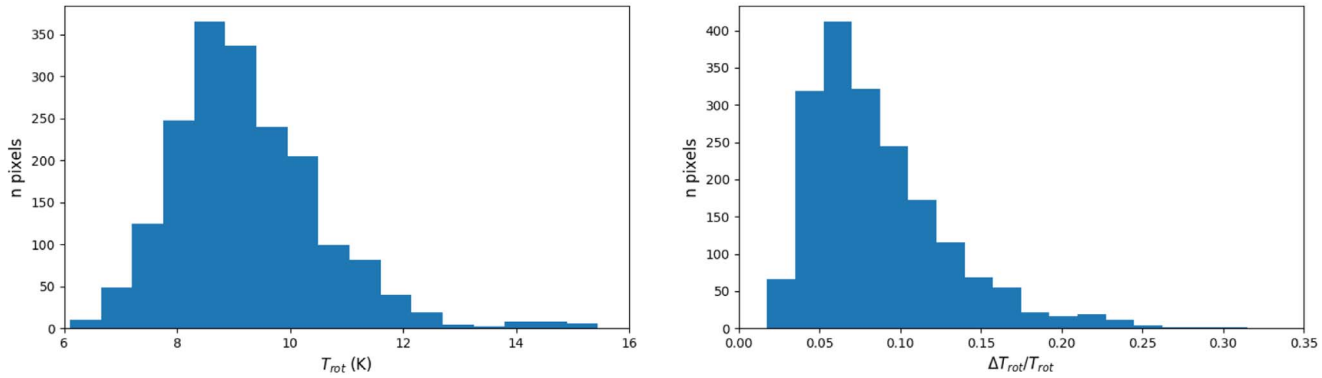

Figure 14. Distribution of $T_{\rm rot}$ based on the rotational diagrams (left) and the distribution of the relative uncertainties $\Delta T_{\rm rot}/T_{\rm rot}$ based on the rotational diagrams (right) of all available points with $S/N > 5$ in the four lines used for the rotational diagrams. Maps of methanol rotational temperatures are available in the .tar.gz package. These maps can be used to recreate Figures 14 and 16.

(The data used to create this figure are available.)

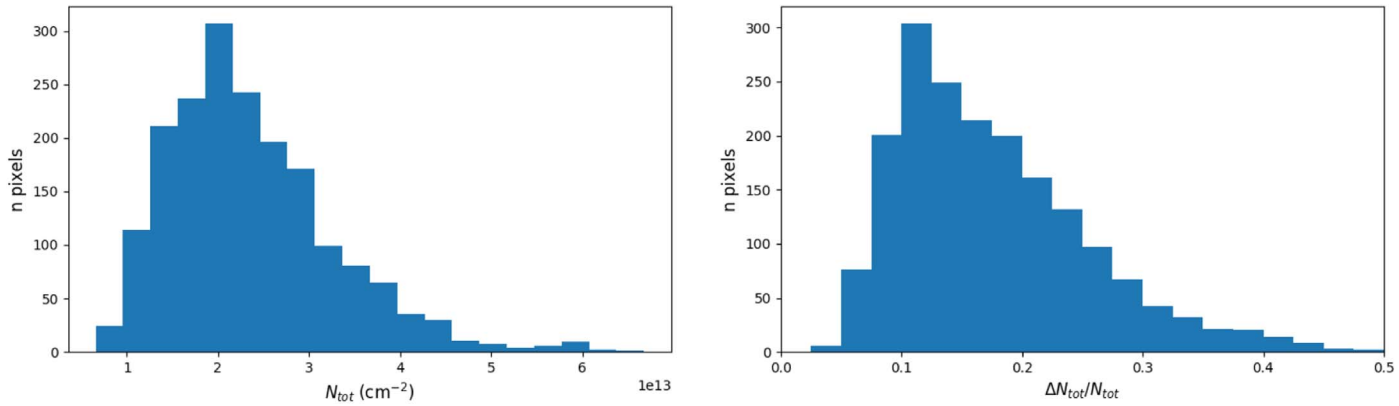

Figure 15. Distribution of $N_{\rm tot}$ based on the rotational diagrams (left) and the distribution of the relative uncertainties $\Delta N_{\rm tot}/N_{\rm tot}$ based on the rotational diagrams (right) of all available points with $S/N > 5$ in the four lines used for the rotational diagrams. Maps of methanol column densities are available in the .tar.gz package. These maps can be used to recreate Figures 15, 17, and 18.

(The data used to create this figure are available.)

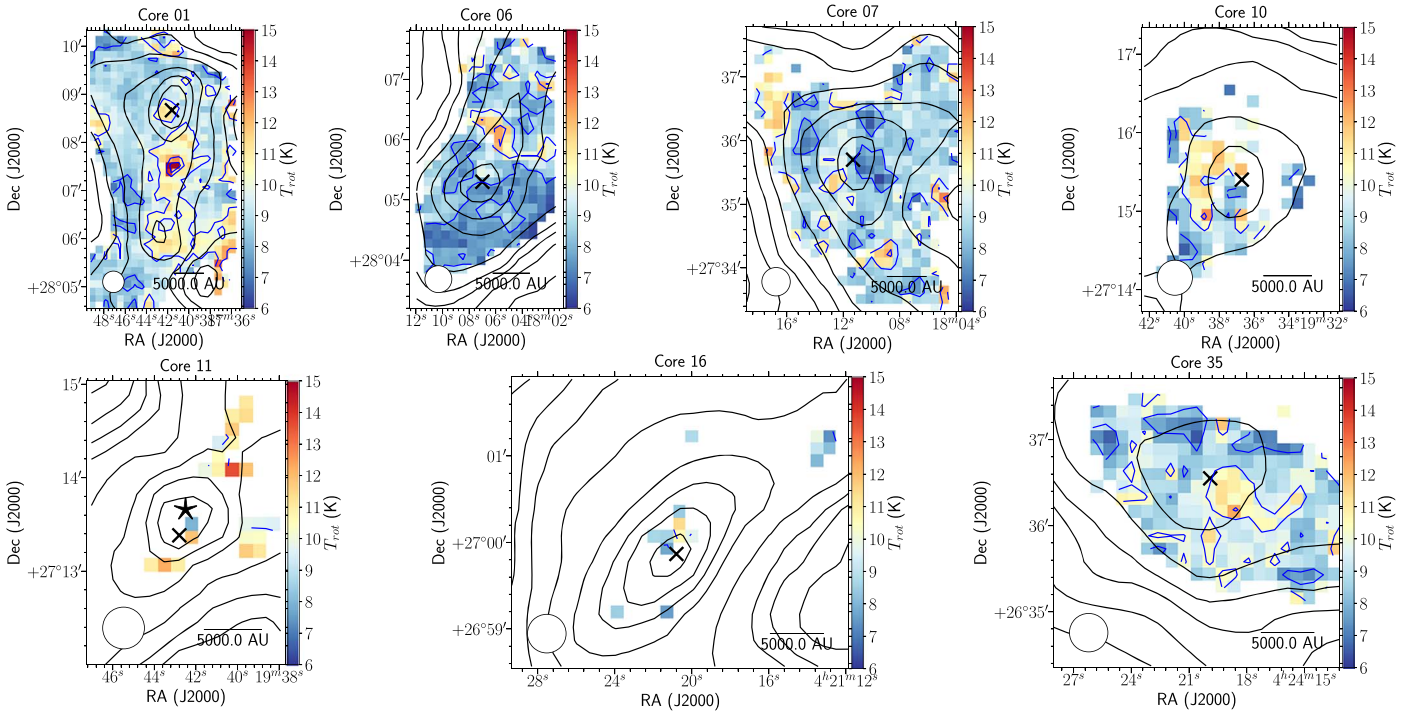

Figure 16. Rotational temperature line toward the observed cores (color scale and blue contours) and visual extinction (black contours at $A_V = 3$, 4, 5, 6, 8, 12, 16, 20, and 24 mag). The top A_V contours are at $A_V = 24$ mag for core 16 and at $A_V = 20$ mag for the other cores. The black star shows the position of Class 0 protostar IRAS 04166+2706 (Santiago-García et al. 2009); crosses show the Herschel/SPIRE dust emission peaks. The white circle at the bottom left of each map shows the 26″ IRAM beam.

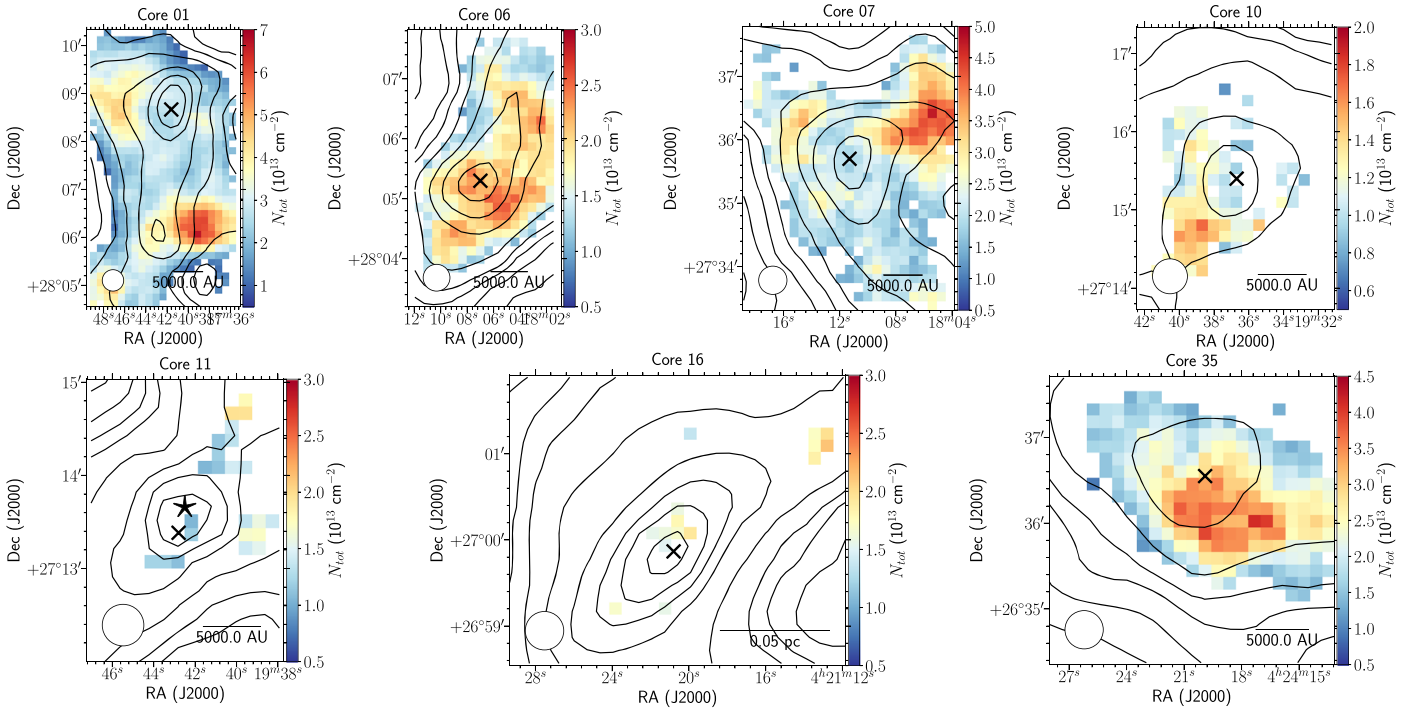

Figure 17. Methanol column densities toward the observed cores (color scale) and visual extinction (black contours at $A_V = 3$, 4, 5, 6, 8, 12, 16, 20, and 24 mag). The top A_V contours are at $A_V = 24$ mag for core 16 and at $A_V = 20$ mag for the other cores. The black star shows the position of Class 0 protostar IRAS 04166+2706 (Santiago-García et al. 2009); crosses show the Herschel/SPIRE dust emission peaks. The white circle at the bottom left of each map shows the 26″ IRAM beam.

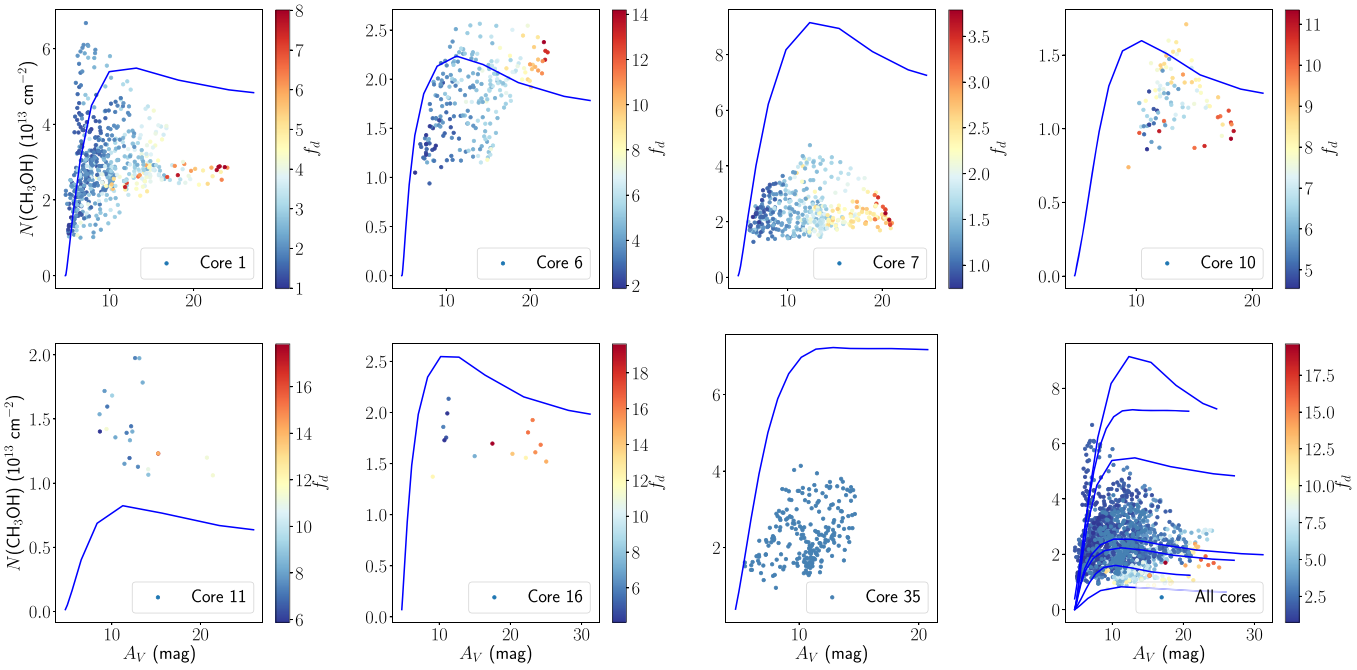

Figure 18. The comparison of the observed (colored dots) and modeled (solid blue line) CH_3OH column density profiles as a function of visual extinction. The color scale represents CO depletion factor f_d. The model includes tunneling for diffusion of H and H_2, and reactive desorption efficiency from Minissale et al. (2016).

ORCID iDs

Anna Punanova https://orcid.org/0000-0001-6004-875X
Anton Vasyunin https://orcid.org/0000-0003-1684-3355
Paola Caselli https://orcid.org/0000-0003-1481-7911
Alexander Howard https://orcid.org/0000-0002-3900-1313
Silvia Spezzano https://orcid.org/0000-0002-6787-5245
Samantha Scibelli https://orcid.org/0000-0002-9485-4394
Jorma Harju https://orcid.org/0000-0002-1189-9790

References

Alonso-Albi, T., Fuente, A., Crimier, N., et al. 2010, A&A, 518, A52
André, P., Di Francesco, J., Ward-Thompson, D., et al. 2014, Protostars and Planets VI (Tuscon, AZ: Univ. Arizona Press), 27
Astropy Collaboration, Robitaille, T. P., Tollerud, E. J., et al. 2013, A&A, 558, A33
Astropy Collaboration, Price-Whelan, A. M., Sipőcz, B. M., et al. 2018, AJ, 156, 123
Bacmann, A., Lefloch, B., Ceccarelli, C., et al. 2002, A&A, 389, L6
Barnard, E. E. 1927, Catalogue of 349 Dark Objects in the Sky (Chicago, IL: Univ. Chicago Press)
Beckwith, S. V. W., Sargent, A. I., Chini, R. S., & Guesten, R. 1990, AJ, 99, 924
Benson, P. J., & Myers, P. C. 1989, ApJS, 71, 89
Bergin, E. A., & Tafalla, M. 2007, ARA&A, 45, 339
Bertin, M., Romanzin, C., Doronin, M., et al. 2016, ApJL, 817, L12
Bizzocchi, L., Caselli, P., Spezzano, S., & Leonardo, E. 2014, A&A, 569, A27
Bracco, A., Palmeirim, P., André, P., et al. 2017, A&A, 604, A52
Caselli, P., Hasegawa, T. I., & Herbst, E. 1994, ApJ, 421, 206
Caselli, P., Walmsley, C. M., Tafalla, M., Dore, L., & Myers, P. C. 1999, ApJL, 523, L165
Caselli, P., Walmsley, C. M., Terzieva, R., & Herbst, E. 1998, ApJ, 499, 234
Caselli, P., Walmsley, C. M., Zucconi, A., et al. 2002, ApJ, 565, 344
Cazaux, S., Carrascosa, H., Muñoz Caro, G. M., et al. 2022, A&A, 657, A100
Chaabouni, H., Bergeron, H., Baouche, S., et al. 2012, A&A, 538, A128
Chacón-Tanarro, A., Caselli, P., Bizzocchi, L., et al. 2017, A&A, 606, A142
Chen, Y. J., Chuang, K. J., Muñoz Caro, G. M., et al. 2014, ApJ, 781, 15
Chuang, K. J., Fedoseev, G., Qasim, D., et al. 2018, ApJ, 853, 102
Crapsi, A., Caselli, P., Walmsley, C. M., et al. 2005, ApJ, 619, 379
Cruz-Diaz, G. A., Martín-Doménech, R., Muñoz Caro, G. M., & Chen, Y.-J. 2016, A&A, 592, A68
Draine, B. T., & Li, A. 2007, ApJ, 657, 810
Fayolle, E. C., Bertin, M., Romanzin, C., et al. 2011, ApJL, 739, L36
Fedoseev, G., Cuppen, H. M., Ioppolo, S., Lamberts, T., & Linnartz, H. 2015, MNRAS, 448, 1288
Fraser, H. J., & van Dishoeck, E. F. 2004, AdSpR, 33, 14
Fredon, A., Lamberts, T., & Cuppen, H. M. 2017, ApJ, 849, 125
Frerking, M. A., Langer, W. D., & Wilson, R. W. 1982, ApJ, 262, 590
Friesen, R. K., Pineda, J. E., co-PIs, et al. 2017, ApJ, 843, 63
Fuchs, G. W., Cuppen, H. M., Ioppolo, S., et al. 2009, A&A, 505, 629
Garrod, R., Park, I. H., Caselli, P., & Herbst, E. 2006, FaDi, 133, 51
Garrod, R. T., Wakelam, V., & Herbst, E. 2007, A&A, 467, 1103
Geppert, W. D., Hamberg, M., Thomas, R. D., et al. 2006, FaDi, 133, 177
Ginsburg, A., & Mirocha, J. 2011, PySpecKit: Python Spectroscopic Toolkit, Astrophysics Source Code Library, ascl:1109.001
Goldsmith, P. F. 2001, ApJ, 557, 736
Goldsmith, P. F., & Langer, W. D. 1999, ApJ, 517, 209
Gordy, W., & Cook, R. L. 1970, Chemical Applications of Spectroscopy, Vol. 2, Microwave Molecular Spectra (New York: Interscience), 1970
Graedel, T. E., Langer, W. D., & Frerking, M. A. 1982, ApJS, 48, 321
Güver, T., & Özel, F. 2009, MNRAS, 400, 2050
Hacar, A., Tafalla, M., Kauffmann, J., & Kovács, A. 2013, A&A, 554, A55
Harju, J., Daniel, F., Sipilä, O., et al. 2017, A&A, 600, A61
Harju, J., Pineda, J. E., Vasyunin, A. I., et al. 2020, ApJ, 895, 101
Hasegawa, T. I., & Herbst, E. 1993, MNRAS, 261, 83
Hasegawa, T. I., Herbst, E., & Leung, C. M. 1992, ApJS, 82, 167
Hasenberger, B., & Alves, J. 2020, A&A, 633, A132
Jiménez-Serra, I., Vasyunin, A. I., Caselli, P., et al. 2016, ApJL, 830, L6
Jiménez-Serra, I., Vasyunin, A. I., Spezzano, S., et al. 2021, ApJ, 917, 44
Jin, M., & Garrod, R. T. 2020, ApJS, 249, 26
Jørgensen, J. K., Schöier, F. L., & van Dishoeck, E. F. 2002, A&A, 389, 908
Keto, E., & Caselli, P. 2008, ApJ, 683, 238
Keto, E., & Caselli, P. 2010, MNRAS, 402, 1625
Kirk, J. M., Ward-Thompson, D., & André, P. 2005, MNRAS, 360, 1506
Laas, J. C., & Caselli, P. 2019, A&A, 624, A108
Lacy, J. H., Knacke, R., Geballe, T. R., & Tokunaga, A. T. 1994, ApJL, 428, L69
Lacy, J. H., Sneden, C., Kim, H., & Jaffe, D. T. 2017, ApJ, 838, 66
Ladjelate, B., André, P., Könyves, V., et al. 2020, A&A, 638, A74
Lamberts, T., & Kästner, J. 2017, ApJ, 846, 43
Lattanzi, V., Bizzocchi, L., Vasyunin, A. I., et al. 2020, A&A, 633, A118
Lee, H. H., Roueff, E., Pineau des Forets, G., et al. 1998, A&A, 334, 1047

Lee, J.-E., Evans, N. J. I., Shirley, Y. L., & Tatematsu, K. 2003, ApJ, 583, 789
Lees, R. M., & Baker, J. G. 1968, JChPh, 48, 5299
Loison, J.-C., Wakelam, V., Gratier, P., & Hickson, K. M. 2020, MNRAS, 498, 4663
Lynds, B. T. 1962, ApJS, 7, 1
Marsh, K. A., Griffin, M. J., Palmeirim, P., et al. 2014, MNRAS, 439, 3683
Minissale, M., Moudens, A., Baouche, S., Chaabouni, H., & Dulieu, F. 2016, MNRAS, 458, 2953
Muñoz Caro, G. M., Chen, Y. J., Aparicio, S., et al. 2016, A&A, 589, A19
Nagy, Z., Spezzano, S., Caselli, P., et al. 2019, A&A, 630, A136
Öberg, K. I., Garrod, R. T., van Dishoeck, E. F., & Linnartz, H. 2009, A&A, 504, 891
Paardekooper, D. M., Fedoseev, G., Riedo, A., & Linnartz, H. 2016, A&A, 596, A72
Pagani, L., Bacmann, A., Cabrit, S., & Vastel, C. 2007, A&A, 467, 179
Palmeirim, P., André, P., Kirk, J., et al. 2013, A&A, 550, A38
Pickett, H. M., Poynter, R. L., Cohen, E. A., et al. 1998, JQSRT, 60, 883
Punanova, A., Caselli, P., Pineda, J. E., et al. 2018a, A&A, 617, A27
Punanova, A., Caselli, P., Feng, S., et al. 2018b, ApJ, 855, 112
Rebull, L. M., Padgett, D. L., McCabe, C.-E., et al. 2010, ApJS, 186, 259
Rimola, A., Taquet, V., Ugliengo, P., Balucani, N., & Ceccarelli, C. 2014, A&A, 572, A70
Roccatagliata, V., Franciosini, E., Sacco, G. G., Randich, S., & Sicilia-Aguilar, A. 2020, A&A, 638, A85
Ruaud, M., Wakelam, V., & Hersant, F. 2016, MNRAS, 459, 3756
Santiago-García, J., Tafalla, M., Johnstone, D., & Bachiller, R. 2009, A&A, 495, 169
Schlafly, E. F., Green, G., Finkbeiner, D. P., et al. 2014, ApJ, 786, 29
Schmalzl, M., Kainulainen, J., Quanz, S. P., et al. 2010, ApJ, 725, 1327
Schnee, S., Enoch, M., Noriega-Crespo, A., et al. 2010, ApJ, 708, 127
Schöier, F. L., van der Tak, F. F. S., van Dishoeck, E. F., & Black, J. H. 2005, A&A, 432, 369
Scibelli, S., & Shirley, Y. 2020, ApJ, 891, 73
Scibelli, S., Shirley, Y., Vasyunin, A., & Launhardt, R. 2021, MNRAS, 504, 5754
Seo, Y. M., Shirley, Y. L., Goldsmith, P., et al. 2015, ApJ, 805, 185
Seo, Y. M., Majumdar, L., Goldsmith, P. F., et al. 2019, ApJ, 871, 134
Shalabiea, O. M. 2001, A&A, 370, 1044
Shingledecker, C. N., Lamberts, T., Laas, J. C., et al. 2020, ApJ, 888, 52
Sipilä, O., Zhao, B., & Caselli, P. 2020, A&A, 640, A94
Spezzano, S., Bizzocchi, L., Caselli, P., Harju, J., & Brünken, S. 2016, A&A, 592, L11
Spezzano, S., Caselli, P., Pineda, J. E., et al. 2020, A&A, 643, A60
Tafalla, M., & Hacar, A. 2015, A&A, 574, A104
Tafalla, M., & Santiago, J. 2004, A&A, 414, L53
Tafalla, M., Santiago-García, J., Myers, P. C., et al. 2006, A&A, 455, 577
Vastel, C., Ceccarelli, C., Lefloch, B., & Bachiller, R. 2014, ApJL, 795, L2
Vasyunin, A. I., Caselli, P., Dulieu, F., & Jiménez-Serra, I. 2017, ApJ, 842, 33
Vasyunin, A. I., & Herbst, E. 2013a, ApJ, 769, 34
Vasyunin, A. I., & Herbst, E. 2013b, ApJ, 762, 86
Wakelam, V., & Herbst, E. 2008, ApJ, 680, 371
Wakelam, V., Loison, J. C., Mereau, R., & Ruaud, M. 2017, MolAs, 6, 22
Walsh, C., Harada, N., Herbst, E., & Millar, T. J. 2009, ApJ, 700, 752
Wannier, P. G. 1980, ARA&A, 18, 399
Ward-Thompson, D., Pattle, K., Kirk, J. M., et al. 2016, MNRAS, 463, 1008
Watanabe, N., & Kouchi, A. 2002, ApJL, 571, L173
Whittet, D. C. B., Cook, A. M., Herbst, E., Chiar, J. E., & Shenoy, S. S. 2011, ApJ, 742, 28
Willacy, K., Langer, W. D., & Velusamy, T. 1998, ApJL, 507, L171
Wilson, T. L., & Rood, R. 1994, ARA&A, 32, 191
Wirström, E. S., Geppert, W. D., Hjalmarson, Å., et al. 2011, A&A, 533, A24
Xu, L.-H., & Lovas, F. J. 1997, JPCRD, 26, 17